Two new multirotor UAVs for glaciogenic cloud seeding and aerosol measurements within the CLOUDLAB project

Anna J. Miller[1], Fabiola Ramelli[1], Christopher Fuchs[1], Nadja Omanovic[1], Robert Spirig[1], Huiying Zhang[1], Ulrike Lohmann[1], Zamin A. Kanji[1], and Jan Henneberger[1]

[1]Institute for Atmospheric and Climate Science, ETH Zurich, Zurich, 8092 Switzerland

Correspondence: Anna J. Miller (anna.miller@env.ethz.ch) and Jan Henneberger (jan.henneberger@env.ethz.ch)

Abstract. Uncrewed Aerial Vehicles (UAVs) have become widely used in a range of atmospheric science research applications. Because of their small size, flexible range of motion, adaptability, and low cost, multirotor UAVs are especially well-suited for probing the lower atmosphere. However, their use so far has been limited to conditions outside of clouds, first because of the difficulty of flying beyond visual line of sight, and second because of the challenge of flying in icing conditions in supercooled clouds. Here, we present two UAVs for cloud microphysical research: one UAV (the measurement UAV) equipped with a Portable Optical Particle Spectrometer (POPS) and meteorological sensors to probe the aerosol and meteorological properties in the boundary layer, and one UAV (the seeding UAV) equipped with seeding flares to produce a plume of particles that can initiate ice in supercooled clouds. A propeller heating mechanism on both UAVs allows for operating in supercooled clouds with icing conditions. These UAVs are an integral part of the CLOUDLAB project in which glaciogenic cloud seeding of supercooled low stratus clouds is utilized for studying aerosol-cloud interactions and ice crystal formation and growth. In this paper, we first show validations of the POPS onboard the measurement UAV, demonstrating that the rotor turbulence has a negligible effect on aerosol measurements. We exemplify its applicability for profiling the planetary boundary layer, as well as for sampling and characterizing aerosol plumes, in this case, the seeding plume. We explain the different flight patterns that are possible for both UAVs, namely horizontal or vertical leg patterns or hovering, with an extensive and flexible parameter space for designing the flight patterns according to our scientific goals. Finally, we show two examples of seeding experiments: first characterizing an out-of-cloud seeding plume with the measurement UAV flying horizontal transects through the plume, and second, characterizing an in-cloud seeding plume with downstream measurements with POPS on a tethered balloon. Particle concentrations and size distributions of the seeding plume from the experiments reveal that we can successfully produce and measure the seeding plume, both in-cloud and out-of-cloud. The methods presented here will be useful for probing the lower atmosphere, for characterizing aerosol plumes, and for deepening our cloud microphysical understanding through cloud seeding experiments, all of which have the potential to benefit the atmospheric science community.

1 Introduction

In situ measurements of the atmosphere, and especially of clouds, are important for understanding and predicting Earth's weather and climate, especially for the energy balance, air quality, hydrological cycle, and other applications. They are needed to calibrate and complement remote sensing measurements to gain a complete perspective on the various elements of the atmosphere. In situ data are also used for initializing and validating weather prediction models important for our daily lives, for example, precipitation forecasts. However, obtaining in situ atmospheric measurements can be challenging, especially in the lower troposphere and in clouds. Uncrewed Aerial Vehicles (UAVs) present one major solution to the challenge of probing the lower troposphere, filling the gap between ground-based and high-altitude measurements. Because UAVs are typically small, cost efficient, reusable, and adaptable for a range of purposes, they can be an excellent addition to the more traditional in situ atmospheric measurement systems like weather balloons and crewed aircraft. Indeed, in recent years UAVs have been increasingly deployed for such purposes. For example, by installing a lightweight optical particle counter or particulate matter sensor, UAVs are well-suited for measuring vertical and/or horizontal distribution of aerosol in the polluted boundary layer (e.g., Weber et al., 2017; Mamali et al., 2018; Samad et al., 2022; Li et al., 2022; Suchanek et al., 2022; Pusfitasari et al., 2023; Järvi et al., 2023). Other examples of UAVs used in atmospheric research include estimating atmospheric turbulence (e.g., Fuertes et al., 2019; Alaoui-Sosse et al., 2019; Egerer et al., 2023), measuring volcanic plumes and their dispersions (e.g., McGonigle et al., 2008; Mori et al., 2016; Albadra et al., 2020), and for meteorological profiling (e.g., Holland et al., 2001; Reuder et al., 2009; Brosy et al., 2017; Koch et al., 2018; Leuenberger et al., 2020; Brus et al., 2021; Bärfuss et al., 2022).

For probing clouds, however, UAVs traditionally face challenges. First, because clouds hinder visibility, it is impossible to fly within visual line of sight into a cloud, and obtaining permission to fly beyond visual line of sight can be difficult due to regulatory frameworks. Second, like conventional crewed aircraft, UAVs can experience significant ice buildup in supercooled clouds, impacting flight performance or leading to a crash. Icing can occur at temperatures below 0 °C and depends on factors such as temperature, liquid water content, ice water content, and cloud droplet size distributions (Bernstein et al., 2005). Ice buildup can occur very quickly on the propellers of a UAV such that the UAV cannot sustain its position and could fly off track or crash down, faster than the pilot can control or prevent it (Catry et al., 2021; Müller et al., 2023). However, one solution to the icing problem on multirotor UAVs is to install heated propellers which can prevent ice from building up, as has been developed for the Meteodrone® (Meteomatics AG, Switzerland, https://www.meteomatics.com/en/meteodrones-weather-drones/). With these Meteodrones, we were able to develop a unique method for in situ glaciogenic cloud seeding and downwind aerosol measurements, even in severe icing conditions.

Glaciogenic cloud seeding is the process of injecting substances into supercooled clouds to initiate primary ice formation. Ice in clouds is important for the atmosphere and climate for several reasons, namely because most continental precipitation is formed via the ice phase (Mülmenstädt et al., 2015; Heymsfield et al., 2020) and because ice crystals affect the radiative properties and lifetime of clouds. Primary ice forms in clouds through two pathways: homogeneous nucleation, where supercooled water spontaneously freezes, or heterogeneous nucleation, where an ice nucleating particle (INP) gives the supercooled water a surface to freeze onto, thereby lowering the energy barrier to ice nucleation (Kanji et al., 2017; Knopf and Alpert, 2023).

Homogeneous ice nucleation can only occur when cloud droplets are supercooled to below -38 °C, whereas heterogeneous nucleation occurs at warmer temperatures, even up to -1 °C, depending on the seed particle type and size (Kanji et al., 2017). In glaciogenic cloud seeding, the heterogeneous ice nucleation process is exploited: particles that are effective INPs are injected into supercooled clouds to artificially initiate ice crystal formation (Dennis, 1980; Rauber et al., 2019). Once the ice crystals
60   form, they grow by vapor deposition and collisions, and may grow large enough to precipitate from the cloud. Therefore, there is interest in cloud seeding as a tool for weather modification but also as a tool for developing our scientific understanding of ice evolution in supercooled mixed phase clouds.

The first glaciogenic cloud seeding experiments were conducted in the 1940s by Schaefer (1946) (using dry ice) and Vonnegut (1947) (using silver iodide particles) followed by a lot of operational cloud seeding activities in the 1970s intending to
65   increase precipitation. However, mixed results of those activities caused waning enthusiasm (see reviews of e.g., Dennis (1980) or Bruintjes (1999)). Currently, despite mixed evidence and continued debates about its efficacy (WMO, 2018; Rauber et al., 2019; Benjamini et al., 2023), there is a renewed interest in cloud seeding with operational seeding projects occurring across the world (e.g., Griffith et al., 2009; Woodley and Rosenfeld, 2004; Kulkarni et al., 2019; Wang et al., 2019; Al Hosari et al., 2021). Some studies, like the SNOWIE project (French et al., 2018; Friedrich et al., 2021), have a strong scientific compo-
70   nent but are attached to operational seeding projects, limiting their experimental possibilities. Further, cloud seeding efforts are usually executed using either crewed aircraft or ground-based seeding techniques to disperse the INPs into clouds, but both pose constraints in terms of cost and flexibility – UAVs can provide a solution to these constraints. A few recent studies have presented methods for operational cloud seeding using fixed-wing UAVs (Jung et al., 2022; DeFelice et al., 2023), which have long flight times compared to multirotor UAVs, but with the sacrifice of precise control. Multirotor UAVs, therefore,
75   are uniquely advantageous for cloud seeding in a scientific perspective, where precision and repeatability are necessary and large-scale seeding is not needed.

In the CLOUDLAB project, we use a multirotor UAV to seed persistent wintertime low stratus clouds as they allow for repeatable glaciogenic cloud seeding and laboratory-like adjustment of experimental parameters (Henneberger et al., 2023). Using a second multirotor UAV equipped with an optical particle counter, we can fly downstream of the seeding location to
80   measure and monitor the seeding plume, while simultaneously measuring the cloud microphysical changes with other in situ and remote sensing instrumentation. Together, the seeding and downstream measurements can help us to better understand aerosol and cloud microphysical processes.

Here we present our novel method for glaciogenic cloud seeding and in situ atmospheric aerosol measurements with two modified, commercial, multirotor UAVs. The measurement UAV can measure particle size distributions and concentrations
85   using an attached Portable Optical Particle Spectrometer (POPS), making the UAV well suited for atmospheric aerosol profiling as well as for measuring and characterizing the plume of seeding particles. The seeding UAV can burn up to two burn-in-place seeding flares while flying in a supercooled cloud with icing conditions, so it can effectively seed cloud regions with temperatures cold enough to glaciate. Both UAVs fly autonomously and have several distinct preprogrammed mission types with adjustable parameters for a range of experiment types (Sect. 2.4), allowing for a variety of flexible and targeted seeding
90   and measurement missions. In the following, we present the capabilities of the measurement and seeding UAVs (Sect. 2),

validation studies for the particle measurements with the measurement UAV (Sect. 3), and the methods for in-cloud and out-of-cloud seeding experiments, with selected results of aerosol particle measurements from the first two CLOUDLAB campaigns (Sect. 5).

2 Instrumentation and field site descriptions

2.1 Meteodrones

95

Both the measurement UAV and the seeding UAV are adapted Meteodrones (MM-670, Meteomatics AG, Switzerland), shown in Fig. 1. These Meteodrones are 6-rotor UAVs with a 70 cm diameter and a weight of 5 kg, able to carry up to 1 kg of instrumental payload. They can fly for approximately 20 minutes at a maximum speed of $10\,\mathrm{m\,s^{-1}}$ and can withstand wind speeds up to $90\,\mathrm{km\,hr^{-1}}$. They were developed to be used for frequent automatic atmospheric meteorological profiling up to

100 6 km above mean sea level (amsl) for the assimilation of their meteorological data into numerical weather prediction models (Leuenberger et al., 2020). The standard version of the Meteodrone is equipped with sensors to measure temperature ($\pm\,0.1$ K), relative humidity ($\pm\,1.8\%$ at $23\,^{\circ}$ C between 0-90% RH), and pressure ($\pm\,1.5$ hPa), as well as a calibrated system for measuring wind speed (uncertainty $<1\,\mathrm{m\,s^{-1}}$) and wind direction (uncertainty $<10^{\circ}$), each at 10 Hz sampling frequency (Meteomatics, personal communication). Meteorological measurements are post-processed by a Meteomatics algorithm to account for sensor

105 calibrations and to combine the data from the ascent and descent flight of a vertical profile.

The Meteodrone MM-670 model features integrated propeller heating to prevent ice from building up on the blades, allowing flights into supercooled clouds. An algorithm in the UAV controller software gives a warning when icing may be occurring according to the real-time UAV temperature and humidity data, but the propeller heating mechanism needs to be activated manually by the pilot. The pilot's decision to activate the propeller heating arises through a combination of assessing the

110 algorithm warning output, the trend of the current battery consumption of the UAV, as well as knowledge and observations of the weather conditions the UAV is experiencing. Upon activation, the propeller heating turns on for 10 seconds. In intense icing conditions, the heating may be activated repeatedly for as long as it is deemed necessary (or until conditions are estimated to be too harsh and the flight is aborted). The downside of the electrothermal deicing mechanism is the high power consumption. Thus, there is a trade-off between the length of flight time and the amount of propeller heating needed, and pilots must be

115 well-trained to handle icing situations appropriately to avoid potential damage or loss of the UAV.

Finally, the Meteodrones are also equipped with an emergency recovery system, including a parachute that is released in emergency situations, for example in the case of engine failure. The Meteodrone parachute system, as well as appropriate pilot training, allows us to obtain airspace permissions to be able to fly beyond visual line of sight in autonomous missions.

2.2 Measurement UAV

120 The measurement UAV (Fig. 1a) is equipped with a Portable Optical Particle Spectrometer (POPS, Handix Scientific, USA). The POPS is a lightweight (550 g) optical particle counter measuring particle number and particle size distribution in the range
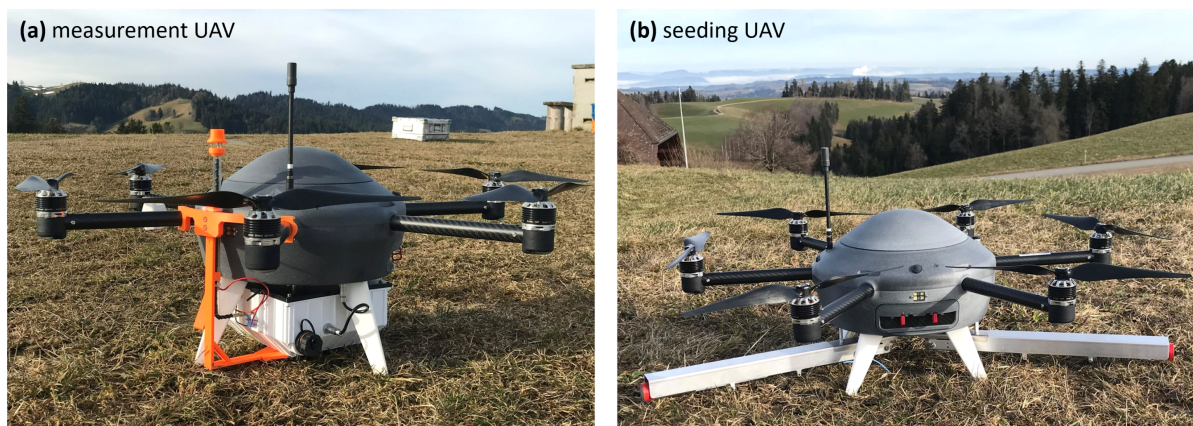
Figure 1. Images of the two UAVs: a) the measurement UAV, a Meteodrone equipped with a Portable Optical Particle Spectrometer (white box) and an extended inlet, and b) the seeding UAV, a Meteodrone with two attached burn-in-place seeding flares.

of 115 nm - 3.37 µm at a 1-second time resolution. POPS was designed to be used on mobile platforms and has already been deployed with success on radiosonde balloons (Yu et al., 2017, 2019; Kloss et al., 2020), tethered balloons (de Boer et al., 2018; Creamean et al., 2021; Pilz et al., 2022; Mei et al., 2022; Walter et al., 2023; Lata et al., 2023), fixed-wing UAVs (Telg et al., 2017; Kezoudi et al., 2021; Mei et al., 2022; DeFelice et al., 2023), and other multirotor UAVs (Liu et al., 2021; Brus et al., 2021).

On our measurement UAV, the POPS (referred to hereafter as $POPS_{UAV}$) is attached to the bottom of the UAV with a custom, 3D-printed, water-tight housing. An inlet extension was designed so that the inlet (1.75 mm inner diameter) extends out of the housing, bends 90° upwards, and extends up to 5 cm above the level of the rotors to avoid their turbulent downwash. The expected losses due to the 90° bend of the inlet are ≤0.03% for particles with ≤4 µm diameter when operating at a flow rate of $3\,\mathrm{cm}^3\,\mathrm{s}^{-1}$ (Brockmann, 2011) and are assumed to be negligible. The inlet also includes a coiled heating wire to prevent the build-up of ice.

2.3 Seeding UAV

The seeding UAV (Fig. 1b) is modified to be able to ignite up to two burn-in-place seeding flares. Attached to the underside of the body of the UAV are two aluminum holders to host the flares. Flare ignition wires are connected to the UAV, and ignition is controlled by the UAV control software which ignites the flare with an electrical pulse at the predetermined ignition point along the seeding pattern. A safety precaution is in place such that the flare will not ignite unless the drone is at least 105 m above ground. When the flare ignites, there is an audible sound, and if out-of-cloud, a visible plume (Fig. 2). The seeding flares we use (Zeus MK2, Cloud Seeding Technologies) are 200 g of material containing a mixture of silver iodide, silver chloride, ammonium salt, and potassium salt, of which around 20 g is ice-active material (Cloud Seeding Technology, personal

communication). One seeding flare burns for 5 - 6 minutes, and we have the option of using up to two flares simultaneously or consecutively.

Figure 2. Image of the seeding UAV hovering at 150 m above ground while an attached flare is burning (out-of-cloud). The photo contrast was enhanced to make the plume more visible.

2.4 UAV flight patterns

The Meteodrone software was modified for us to be able to fly our desired seeding and measurement patterns. Both the measurement and seeding UAV can autonomously fly predefined flight patterns, and all patterns can be performed either in-cloud or out-of-cloud. The execution of the flight patterns is entirely autonomous, with the pilot only needing to "launch" the mission after completing a pre-flight checklist (e.g., checking weather, airspace clearance, the physical UAV itself, and its battery), as well as to activate deicing as needed.

The parameter space available to us in configuring a mission, where a "mission" is considered one complete flight by a UAV, is illustrated in Fig. 3. First, during the experiment planning stage, we observe the prevailing environmental conditions using a combination of remote sensing and in situ measurements to choose an appropriate altitude and location for seeding. The most important variables for our decision are wind speed, wind direction, cloud base altitude, cloud top altitude, temperature profile within the cloud, and cloud structure (i.e., cloud radar reflectivity). When we have determined the ideal seeding altitude, the prevailing wind speed and direction, and our desired flight pattern, we use a custom-programmed website interface to calculate the seeding pattern start coordinates (x_1, y_1, and z_1 in Fig. 3) and UAV flight speed (v_1), as well as the best launch site, which is chosen from a set of pre-selected UAV launch locations surrounding our main measurement site (more details can be found in Henneberger et al., 2023). Our seeding pattern can be any number of horizontal or vertical legs (n), with any length of leg (L), and any horizontal distance between legs (dx), within our airspace allowance. Additionally, we can set a waiting time after each leg (t_{wait}), which is useful in the case where we want the UAV to remain stationary while seeding (parameters $n = 1$, $L = 0$, and $dx = 0$ with $t_{wait} = 5$ minutes). Finally, there is a parameter to set whether to ignite the first seeding flare and if/when to ignite the second flare. The first seeding flare ignites (if set to do so) when the UAV reaches the pattern start point

(x_1, y_1, z_1), while the second flare ignition point can be set to the start of a specified leg. The flight patterns and parameter space are used for designing the flight pattern of both UAVs; all parameters are the same for a measurement mission except the flare ignition. Based on these parameters, we can flexibly design experiments to suit the current environmental conditions and our different scientific questions.
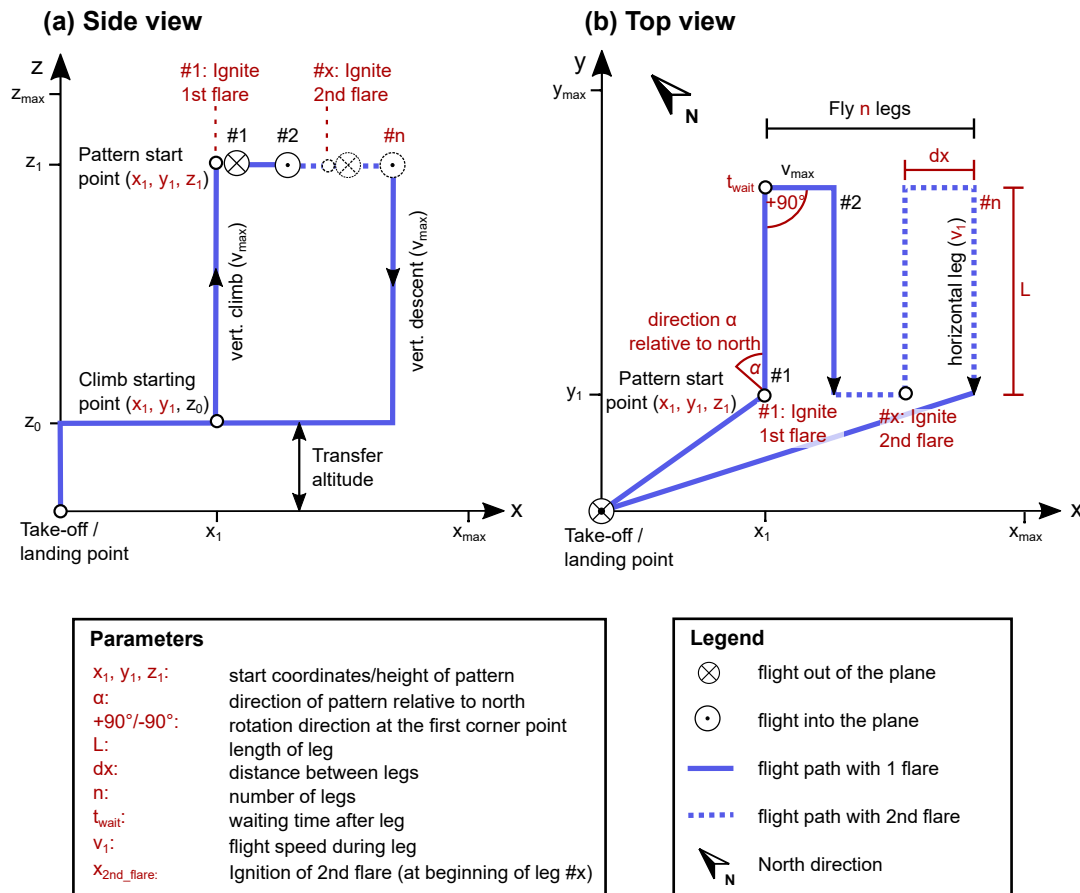
Figure 3. A schematic illustrating the parameter space for programming a horizontal seeding mission, in which the seeding UAV flies legs perpendicular to the wind direction (e.g., northwest winds implied here) at the same altitude while seeding, with a) the side view and b) the top view. The same parameter space is used to program vertical seeding missions, in which the seeding UAV flies legs vertically.

165

2.5 CLOUDLAB field site and other instrumentation

The CLOUDLAB project has had two wintertime measurement field campaigns, in January 2022 - March 2022 and in December 2022 - February 2023, and a third campaign is planned for December 2023 - February 2024. The main field site of the campaigns is in the central Swiss Plateau region in Eriswil, Switzerland (main site coordinates: 47°04'14"N, 7°52'22"E, 170   920 m elevation). We obtained air space clearance for our experiments with an area of a 4 km radius and a 2 km amsl height

(1080 m above ground relative to the main site). At the main measurement site, we have a suite of in situ and ground-based remote sensing instrumentation, detailed in Henneberger et al. (2023).

Remote sensing instruments relevant to the results presented here include: a ceilometer (CHM 15K, Lufft) for detecting cloud base height and planetary boundary layer height, a cloud radar (Mira-35, Metek) for detecting cloud top and cloud structure, and a radar wind profiler (LAP-3000, Vaisala) provided by MeteoSwiss for measuring vertically-resolved wind speeds and directions.

Relevant in situ devices are radiosondes (Sparv S1H3, Windsond) for obtaining vertical profiles of temperature, humidity, and wind, as well as a tethered balloon system (TBS). The TBS has a measurement platform with a holographic imager to measure cloud droplets and ice crystals (Ramelli et al., 2020), and was extended to include a POPS onboard (referred to hereafter as POPS$_{TBS}$) for measuring aerosol. The instrumentation aboard the TBS is used during in-cloud seeding experiments to detect and measure the aerosol particles of the seeding plume, cloud droplets, and ice crystals. Here, only the aerosol particle measurements will be discussed (other data related to seeding experiments are presented in Henneberger et al., 2023).

3 Validation of POPS measurements on the measurement UAV

The POPS has been extensively described, characterized, and validated in previous studies (Gao et al., 2016; Mei et al., 2020; Liu et al., 2021; Mei et al., 2022; Kasparoglu et al., 2022; Pilz et al., 2022; Mynard et al., 2023). Here, we performed selected tests in the laboratory to ensure that POPS$_{UAV}$ and POPS$_{TBS}$ count and size particles correctly, detailed in Appendix A. Briefly, the two POPS were compared while measuring polystyrene latex spheres of size 246 and 522 nm; they both measured the particles in the correct size bin and by comparing their relative concentrations, we obtain an estimate of instrument variability of 30% (Fig. A1). Additionally, by comparing POPS$_{TBS}$ measurements with simultaneous measurements from a Scanning Mobility Particle Sizer and an Aerodynamic Particle Sizer, we obtain an estimate for uncertainty in concentration of 50% for all particle sizes (Fig. A2).

To further validate POPS$_{UAV}$, we investigated the effects that the rotors have on the aerosol measurements (Sect. 3.1 and 3.2), and defined a new way of ensuring good data quality of high-concentration measurements (Sect. 3.3 and Appendix C).

3.1 Comparison of POPS measurements with and without rotors

Previous studies have demonstrated the ability to obtain high-quality aerosol measurements from a POPS mounted on a multi-rotor UAV (Liu et al., 2021; Brus et al., 2021). Characterizing and validating the measurements obtained from a multirotor UAV is important to quantify any effects that the rotors may have on particle measurements. Since the rotors can produce significant downwash and turbulence, the flow into the aerosol inlet may be affected (Alvarado et al., 2017). To help assess whether there are influences on POPS measurements while our UAV is flying, we designed two experiments to compare measurements with and without rotors.

In the first experiment, we compared 5-minute particle size distributions measured while the measurement UAV was hovering at approximately 3 m above ground to the particle size distributions measured while the UAV was standing on top of a trailer,
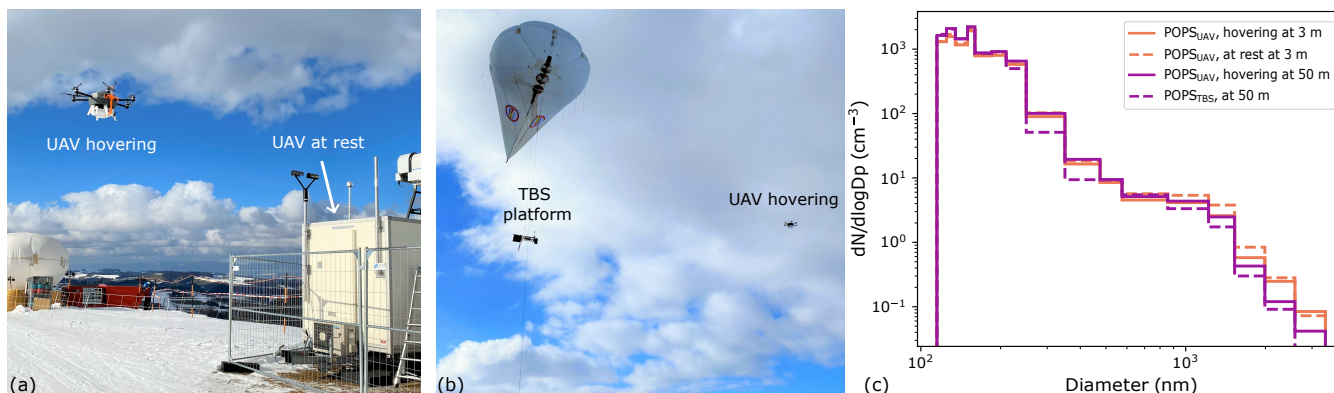
Figure 4. a) Image of the measurement UAV hovering beside a trailer during the rotor comparison experiment. The sampling position without rotors is indicated by the arrow. b) Photograph of the TBS flying with its measurement platform containing $POPS_{TBS}$, while the measurement UAV hovers approximately 20 m away at the same altitude (50 m above ground). c) $POPS_{UAV}$ size distributions from the UAV hovering at 50 m above ground (purple, solid line) compared to size distributions from $POPS_{TBS}$ also at 50 m above ground (purple, dashed line); $POPS_{UAV}$ measurements from when the UAV hovered at 3 m above ground (orange, solid line) compared to when the UAV was 3 m above ground at rest atop the trailer roof (orange, dashed line). Size distributions are taken over the 5-min length of each experiment.

with rotors off, also at a height of approximately 3 m above ground (Fig. 4a). The resulting size distributions indicate good agreement (Fig. 4c), i.e., no detectable difference between the POPS measurements obtained during hovering and standing

205 phases when including instrument variability of 30% (see Appendix A), revealing that the turbulence of the rotors likely does not affect the particle measurements.

In the second experiment (one hour after the first), we compared measurements from $POPS_{UAV}$ to measurements from $POPS_{TBS}$. Both POPS simultaneously sampled air at approximately 50 m above ground with approximately 20 m horizontal distance between them, for 5 minutes (Fig. 4b). In this way, we could compare POPS size distributions from the in-flight UAV

210 to a POPS with no turbulent rotors near the inlet. The results again indicate no appreciable difference between the two size distributions (Fig. 4c), supporting the conclusion of no detectable impact of the rotors on $POPS_{UAV}$ measurements.

3.2 Comparison of POPS measurements during ascending and descending profiles

Another way to identify possible influences of the turbulent downwash from the rotors on the aerosol flow is to compare the ascent and descent measurements of vertical profiles (Liu et al., 2021; Fuertes et al., 2019), because on the descent, the UAV

215 flies through its own downwash. 34 vertical profiles to 1000 m above ground were performed by the measurement UAV during the first two winter campaigns. Particle number concentration measurements were compared between the ascent and descent of each vertical profile (all profiles are in Appendix B). The ascending and descending speed is approximately $10\,\mathrm{m\,s^{-1}}$, thus the total flight time in these profiles is approximately 3 min, and therefore the true atmospheric composition is expected to be the same in both directions for any given profile. Qualitatively, the ascent and descent measurements usually agree well

220   with each other under many different atmospheric conditions (Fig. B1). Sometimes the descent flight measurements have more variability than the ascent flight (e.g., in flight 2022-03-09 13:22, Fig. B1), likely due to a small influence of rotor turbulence or flight instabilities. However, as can be seen in the quantitative assessment described below, these variabilities do not affect the mean concentrations.

    To quantitatively assess differences in ascent and descent particle number concentration (Fig. 5), the particle concentration

225   measurements were first binned into altitude intervals of 100 m then averaged over each interval on the ascent and the descent of each flight. Particle counts from the smallest size bin (115 - 125 nm) were excluded, as it is known that the first bin may have considerably higher inaccuracies (e.g., Mei et al., 2020; Pilz et al., 2022), a common issue with optical particle counters. Additionally, there were 9 outlier data points excluded from the raw data (of 9113 total) due to extremely unrealistic concentrations (3000 - 50000 $\mathrm{cm^{-3}}$; outliers can be seen in profiles in Fig. B1).
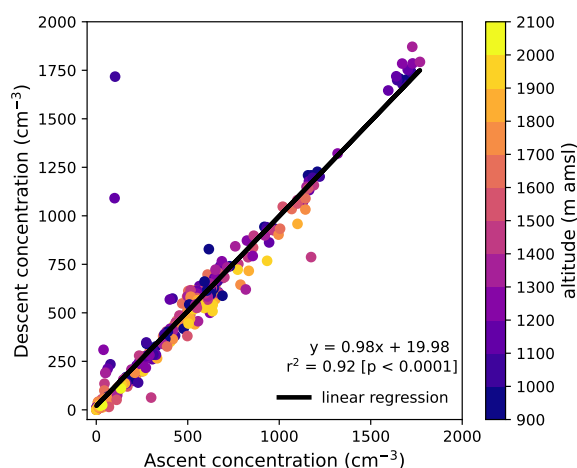
Figure 5. Particle concentrations measured on the ascent versus the descent of 34 vertical profiles by the measurement UAV, colored by their altitude. Measurements from each vertical profile were binned into twelve 100 m altitude intervals, and concentrations were averaged over each altitude interval. The black line is the linear regression through the data.

230   The means of the ascent and descent are in very good agreement across all concentrations and all altitude bins (Fig. 5). Two outliers with high descent and low ascent concentration are the result of a single profile flight with unusual concentrations (see profile on 2022-01-28 14:02 in Fig. B). Nevertheless, the linear regression of all data has a slope of near unity (0.98) with a Pearson correlation coefficient of 0.92 (p-value < 0.0001). Since the measurements obtained from the ascents and descents are in good agreement, the impact of the rotor downwash on the POPS measurements can be neglected.

235 **3.3 Data quality filter for POPS measurements at high concentrations**

Every particle measurement device, including POPS, has an upper concentration limit above which it does not count and size particles accurately, due to counting limits and coincidence errors (Gao et al., 2016). For POPS, there is not yet a consensus

on what concentrations still give data that are acceptable and trustworthy. For our purposes, where we use POPS to measure a highly concentrated plume of aerosol (up to 15,000 particles cm^{-3}; Sect. 5.1 and 5.2), we defined a new way to filter out data

240   using the POPS "baseline", a measure of the background scattering signal. Appendix C details this data flagging and filtering method which we apply to all POPS measurements to ensure good data quality.

4   Estimating the boundary layer height with the measurement UAV: a case study

One possible application of the measurement UAV is to profile and characterize the planetary boundary layer (PBL), which is of importance for weather predictions and air pollution modeling. There are several methods for determining the height

245   of the PBL, such as finding the minimum gradient in a vertical profile of relative humidity or aerosol concentration (e.g., Summa et al., 2022; Jozef et al., 2022). Vertical profiles of the aerosol concentration can either be derived from attenuated
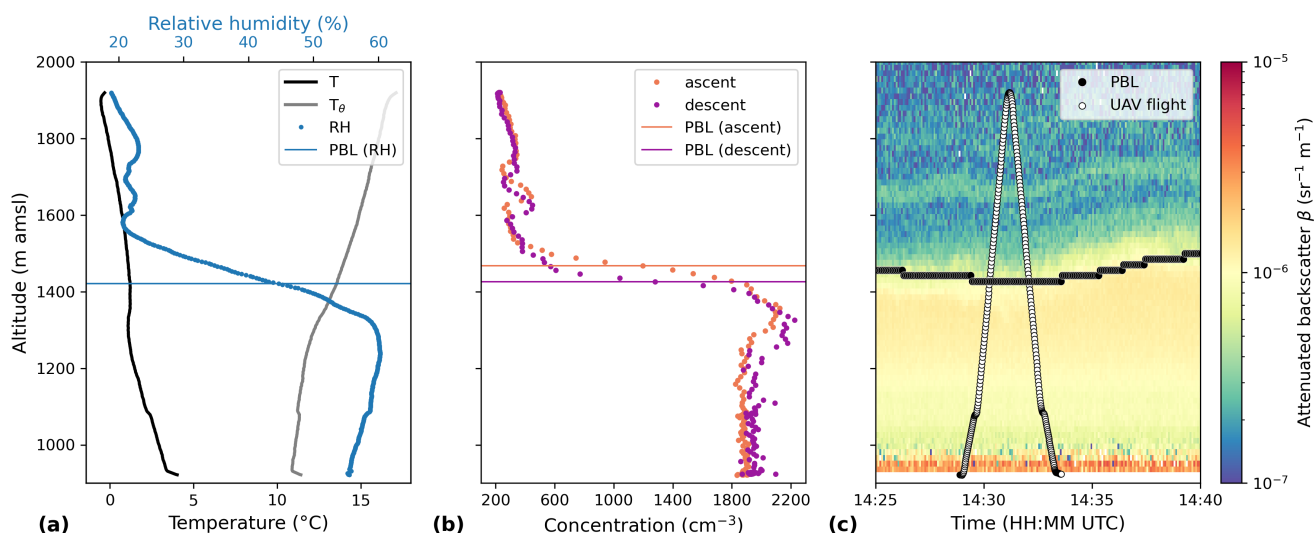
Figure 6. Height-resolved meteorological and aerosol properties captured by the measurement UAV on 8 March 2022 at 14:28 UTC, compared to co-located ceilometer backscatter data. a) Temperature (black), relative humidity (blue), and potential temperature (grey) profiles were measured by the Meteodrone sensors mounted on the measurement UAV and post-processed with a Meteomatics algorithm to calibrate and combine the ascent and descent data. The horizontal blue line at 1421 m indicates the PBL height based on the RH gradient. b) POPS$_{\text{UAV}}$ particle concentrations measured during the ascent (orange) and descent (purple) flight of the UAV. Horizontal orange and purple lines at 1467 m and 1426 m indicate the PBL heights based on the gradient of the ascent and descent particle concentration, respectively. c) Attenuated backscatter β time series measured by the ceilometer, with black circles for the detected PBL height based on the gradient of the attenuated backscatter and white circles for the UAV flight path.

backscatter lidar measurements, as is commonly done with ceilometers, or aerosol concentration can be directly measured with vertically-resolved in situ measurements, like POPS on a UAV.

We present one example of a vertical profile up to 1000 m above ground by the measurement UAV on 8 March 2022 at
14:28 UTC at the CLOUDLAB main measurement site, compared to a time series of attenuated backscatter measurements from
a ceilometer at the same location and time (Fig. 6). The PBL height is calculated from the ceilometer data by the manufacturers
algorithm (Lufft). At the time of the UAV flight, the reported PBL height was at 1440 m amsl during both the ascent and descent
flights. Similarly, the relative humidity measured by the UAV (Fig. 6a) indicates a PBL height of 1421 m amsl (calculated as
the minimum gradient of relative humidity), only 19 m different from the ceilometer. Likewise, in the POPS$_{UAV}$ data, the
particle concentration profile had a minimum concentration gradient at 1467 m amsl for the ascent flight and 1426 m amsl
for the descent flight (Fig. 6b) – just a 27 and 14 m difference, respectively, from the ceilometer-derived PBL height. These
differences are small compared to the general disagreement between PBL detection methods (Collaud Coen et al., 2014), and
also likely lies within the uncertainty of POPS or the ceilometer. Furthermore, in both the POPS$_{UAV}$ and the ceilometer data,
we can identify a thin layer of higher aerosol concentration at approximately 1650 m amsl. This case study illustrates that the
measurement UAV can characterize the lower atmosphere as well as a ceilometer, with the advantage that it has co-located
meteorological measurements and that it can be easily deployed at different locations.

5 Usage of UAVs for seeding experiments

We have shown that the measurement UAV can accurately and flexibly measure aerosol in the lower atmosphere. Next, we
show how the measurement UAV with POPS$_{UAV}$ can be used to characterize the dispersion of an out-of-cloud seeding plume
produced by the flares on the seeding UAV (Section 5.1 and Fig. 7a). Then, we present an in-cloud seeding experiment with
the seeding UAV in a supercooled cloud with downstream measurements by POPS$_{TBS}$ (Section 5.2 and Fig. 7b).

5.1 Characterizing an out-of-cloud seeding plume with POPS on the measurement UAV

During an out-of-cloud stationary seeding mission (illustrated in Fig. 7a), the seeding UAV burns the seeding flares while
hovering stationary at the defined altitude, while the measurement UAV flies horizontal legs through the seeding plume. These
missions can be flown autonomously, but here we present a case in which the measurement UAV was manually controlled to
fly transects through the seeding plume (Fig. 8). This seeding mission was performed on 28 March 2022 at 9:30 UTC under
clear-sky conditions. Seeding altitude was 1320 m asl, with a temperature of 9.5 °C, a wind speed of 7 m s^{-1}, and a wind
direction of 240° (measured in agreement by radiosonde and UAV profile). The seeding UAV hovered at the seeding altitude
while two consecutive flares burned, while the measurement UAV flew transects perpendicular to the wind direction at six
different distances (80 - 370 m) downwind of the seeding location (Fig. 8). At each distance downwind, between two and nine
legs were flown through the plume. Because of the small distance between the seeding location and the measurement UAV, the
plume was highly concentrated (more than 15,000 particles cm^{-3}) and thus needed to have some data filtered out (31 of 104
in-plume data points), according to the data filter method introduced in Sect. 3.3.

The concentration-colored flight path (Fig. 8) shows that elevated concentrations, up to 1.5 orders of magnitude above the
background, were measured along the prevailing wind direction downwind of the seeding UAV. However, there was significant
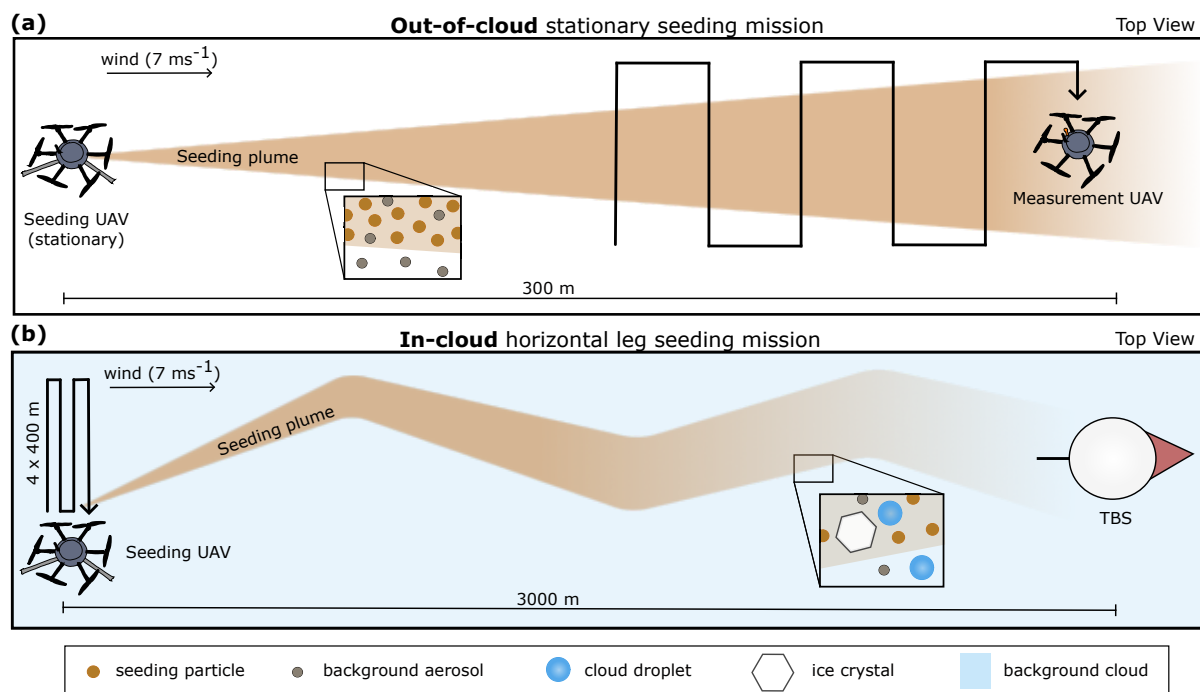
Figure 7. Illustration of two example seeding missions, from a top-down view (not to scale). a) An out-of-cloud stationary seeding mission, in which the seeding UAV hovers stationary at a constant altitude while burning a flare, while the measurement UAV flies horizontal transects through the plume. The inset illustrates that the seeding plume contains seeding particles and background aerosol, whereas outside the plume there is only background aerosol. b) An in-cloud horizontal leg seeding mission (blue background is the background cloud), in which the seeding UAV flies 4 horizontal legs of each 400 m, 3000 m upstream of the TBS. The distance between legs is shown for illustration purposes; often the legs are performed at the same place. The inset illustrates that the seeding plume contains seeding particles, cloud droplets, ice crystals, and background aerosol, whereas outside the plume there are background aerosol and cloud droplets. In all experiments, the UAVs and the TBS fly at the same altitude.

variability in the location and magnitude of concentration peaks. Viewing concentration as a function of distance from the expected plume center line (see arrows in Fig. 8) for four downwind distances (144, 210, 250, and 300 m) illustrates the variability in the plume measurements (Fig. 9). First, note that not all transects measured concentrations above the background, indicating that some of the transects were not actually through the plume. Therefore, the plume itself must have been displaced horizontally or vertically because the transects at each downwind distance were flown at the same location. Plume displacement is also evident when considering the center of each plume peak – most peaks are not centered at 0 m, and at 300 m downwind, the peaks are horizontally displaced by 50 or 100 m. Second, there are considerable dissimilarities in the width and height of each concentration profile. These dissimilarities occur both between transects at the same downwind location and between different downwind locations. Interestingly, there is no consistent trend with increasing downwind distance in terms of concentration magnitude or peak width, contrary to what would be expected according to Gaussian dispersion (i.e., decreasing concentration
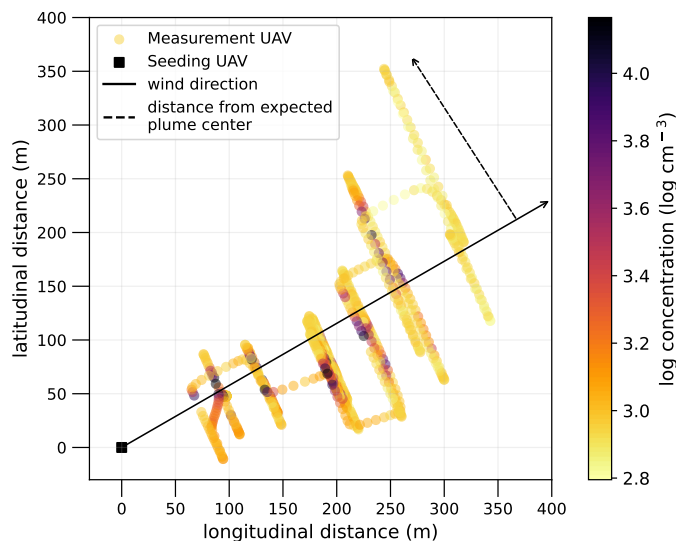
Figure 8. The flight path of the measurement UAV in relation to its longitudinal and latitudinal distance from the seeding UAV, colored by the particle concentration measured by $POPS_{UAV}$, during the out-of-cloud seeding mission on 28 March 2022. The solid line arrow indicates the mean wind direction during the mission. The dashed arrow shows distance from expected plume center, which is used as the x-axis in Figure 9.

and increasing peak width with increasing distance downwind). These measurements indicate the turbulence within the seeding plume and generally illustrate the unpredictable nature of the dispersion of particles in a plume. Indeed, because of the complexities of turbulence, accurately modeling atmospheric particle dispersion is known to be difficult (e.g., Shirolkar et al., 1996; Holmes and Morawska, 2006), especially on small spatial and time scales as we measure here. The method presented
295 here provides a potential framework for further quantitative experimental investigations into aerosol dispersion, relevant for air pollution modeling and other applications.

5.2 Characterizing an in-cloud seeding plume with POPS mounted on the TBS

In an in-cloud horizontal leg seeding mission (Fig. 7b), the seeding UAV flies horizontal legs perpendicular to the wind direction, upstream of the TBS, within a supercooled cloud. Because the seeding pattern is perpendicular to the wind direction,
300 the seeding plume creates a zig-zag shape as it gets transported toward the TBS, and the signal measured by the TBS is then expected to be multiple distinct signals corresponding to each of the seeding legs. The seeding plume in-cloud is expected to contain a mixture of supercooled cloud droplets (from the pre-existing cloud and/or newly created droplets from seeding particles that activated as cloud condensation nuclei), ice crystals (from the pre-existing cloud and/or nucleated by seeding particles acting as ice nucleating particles), and the remaining un-activated/un-nucleated seeding particles. $POPS_{TBS}$ measures
305 these leftover seeding material particles, while the holographic imager measures the cloud droplets and ice crystals (not shown
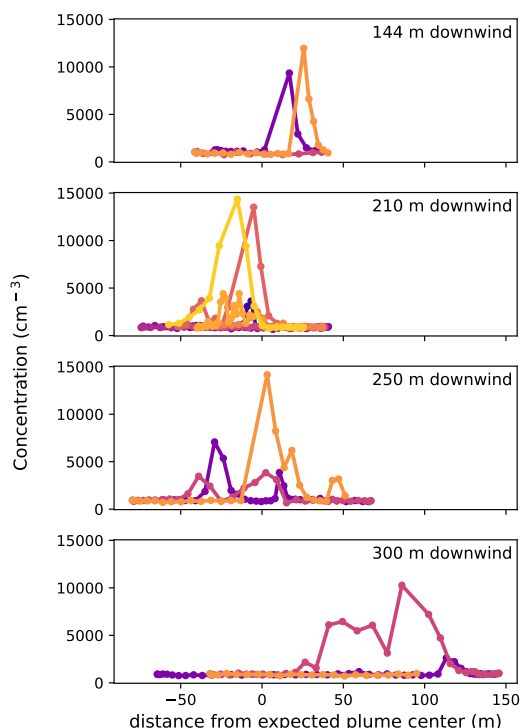
Figure 9. Particle concentrations in the seeding plume as a function of distance from expected plume center (see arrows in Fig. 8), for the out-of-cloud seeding mission on 28 March 2022. Concentration was measured by POPS$_{UAV}$ while the measurement UAV flew transects nearly perpendicularly through the seeding plume at several distances downwind of the seeding UAV (144 m, 210 m, 250 m, 300 m). At 144 m, 250 m, and 300 m, three transects were made, and at 210 m downwind, nine transects were made. Individual transects are distinguished by color; their color is otherwise meaningless.

here). Although the measurement UAV was not operated during in-cloud seeding missions in the CLOUDLAB campaigns of 2021-22 and 2022-23 due to logistical reasons, in future campaigns the measurement UAV will be used as an additional measurement of the in-cloud seeding plume in between the seeding UAV and the TBS.

The in-cloud seeding mission we present here was conducted at 19:45 UTC on 24 January 2023. On this day, the measure-

310   ment site was covered with a persistent low stratus cloud, and at the time of the experiment, the cloud base was at approximately 1000 m asl (measured by the ceilometer) and cloud top at 1600 m asl (measured by the cloud radar). The seeding altitude was chosen as 1350 m asl, with a temperature of −5.1 °C (measured by the seeding UAV). At the seeding height, the wind direction was 77° with a speed of $7 \, \mathrm{m \, s^{-1}}$ (measured by the radar wind profiler and a radiosonde), with wind direction further confirmed by the angle at which the TBS oriented itself in the wind relative to its anchor position. The seeding UAV flew four 400 m legs,

315   with no distance between legs, 3000 m upwind of the TBS measurement platform (similar to Fig. 7b). The seeding flare ignited at 19:44:46 UTC and the seeding pattern ended at 19:50:26, for a total estimated burning time of 5 minutes and 40 seconds.
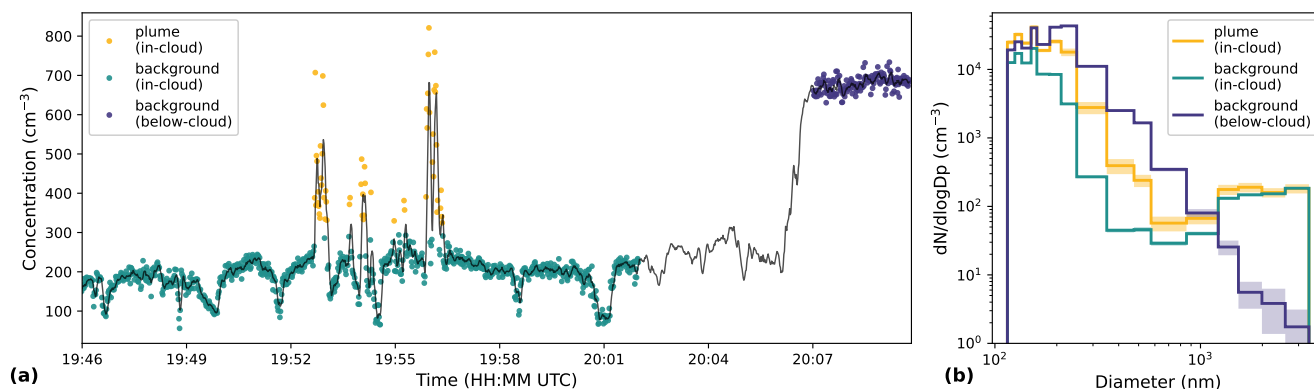
Figure 10. (a) Time series of total particle concentration measured by POPS$_{TBS}$ (solid line is a 5-second moving average of the 1-second data points) from the in-cloud horizontal leg seeding mission on 24 January 2023 when the seeding UAV flew 4 legs of each 400 m, 3000 m upwind of the TBS measurement platform. Yellow markers indicate when POPS$_{TBS}$ measured the seeding plume in-cloud (defined as total concentration $> 370 \, \text{cm}^{-3}$ while in cloud), green markers for when POPS$_{TBS}$ was measuring the background in-cloud (total concentration $< 340 \, \text{cm}^{-3}$ while in cloud), purple markers for when POPS$_{TBS}$ measured background below-cloud, and no markers for when the TBS was transitioning between altitudes. (b) Size distributions of the three situations: the seeding plume in-cloud (yellow), the background in-cloud (green), and the background below-cloud (purple), corresponding to the data markers in panel a. Shading around the mean represents one standard deviation.

This seeding mission was unique in that the TBS was brought back to ground immediately after the experiment, thus allowing POPS$_{TBS}$ to measure three different conditions in a short period of time: the background supercooled stratus cloud, the seeding plume in-cloud, and the background below the cloud. The seeding plume signal ($370 - 800 \, \text{cm}^{-3}$) stands out clearly from the

320   in-cloud background ($100 - 340 \, \text{cm}^{-3}$) by the elevated particle concentrations during the passage of the seeding plume (Fig. 10). In fact, four distinct groups of peaks can be seen, corresponding to the four legs of the seeding pattern. The first signal appears at 19:52:39 and the last signal ends at 19:56:22, for a total duration of 3 minutes 43 seconds, starting 7 minutes 53 seconds after the flare was ignited. Based on the estimated local wind speed and the distance between seeding and measuring, the calculated advection time of the seeding particles is 6 minutes 58 seconds; i.e., we would expect to see the signal in

325   POPS$_{TBS}$ approximately 7 minutes after seeding started, in the absence of turbulence. Therefore, the elevated concentrations that POPS$_{TBS}$ measured are highly likely to be the seeding plume passing by. Furthermore, small deviations in the timing compared to the calculated timing are expected due to uncertainties in wind measurements as well as variability and turbulence in the 3000 meters between seeding and measuring. Turbulence and mixing within the cloud are also demonstrated by the fact that there is significant variability in the seeding concentration and the time spans of the seeding signals (Fig. 10), similar to

330   the findings from the out-of-cloud seeding case discussed previously.

Particle size distributions for each of the three situations (plume in-cloud, background in-cloud, and background below-cloud) are shown in Fig. 10b. As compared to the in-cloud background, the seeding plume had 2 - 10 times more particles

with sizes between 165 and 1220 nm, but a similar number of particles of size > 1220 nm. In contrast, the below-cloud background had 6 - 75 times fewer particles > 1220 nm than the in-cloud, but 2 - 60 times more particles < 1220 nm. These size

335 distributions indicate that the > 1220 nm particles $POPS_{TBS}$ measured in-cloud were likely small cloud droplets, since they were not present in the below-cloud measurement and were present in similar amounts in both the in-cloud seeding plume and in-cloud background. It is also notable how the total number of particles in the below-cloud measurement (approx. $700\,cm^{-3}$) was significantly higher than the in-cloud background (up to $340\,cm^{-3}$), showing the effects of particle activation into cloud droplets as well as scavenging of aerosol particles by cloud droplets.

340 Finally, it is important to note that the in-cloud background had large fluctuations in concentration ($50 - 340\,cm^{-3}$, Fig. 10a). These fluctuations were present in $POPS_{TBS}$ in-cloud measurements in around half of all the in-cloud seeding missions and were likely caused by moisture build-up in the POPS inlet. The moisture may interfere with the air inflow or with the optical measurement itself. The issue can be solved by running POPS in clean, dry conditions for a few minutes between experiments. When taking these steps in our next measurement campaign, we can obtain more consistent measurements. Nonetheless, in the

345 measurements we have so far, this issue was usually not severe enough to mask the seeding signal from the background.

6   Discussion and Conclusions

This paper presented two new UAVs: a seeding UAV equipped with burn-in-place flares and a measurement UAV equipped with a Portable Optical Particle Spectrometer, both able to fly into supercooled clouds. We introduced the flight patterns of the measurement and seeding UAV with the parameter space available to configure the flight missions. We then showed that

350 the POPS data on the measurement UAV are comparable to other aerosol instrument measurements and are likely not influenced by rotor-induced turbulence from the UAV. Finally, we demonstrated POPS measurements from selected experiments to demonstrate how we can successfully measure the boundary layer and a seeding plume in and out-of-cloud. We see the following three major applications, discussed below.

First, the measurement UAV can be used for profiling the atmosphere, i.e., measuring temperature, humidity, wind, and parti-

355 cle size distributions. In Section 4, a measurement UAV profile was compared to the backscatter measurements from a ceilometer, showing a similar trend in $POPS_{UAV}$ particle concentrations as the ceilometer with respect to height. This case demonstrates how the UAV serves as a more flexible alternative for characterizing the lower atmosphere. Additionally, the propeller heating and the flight time of around 20 minutes allow for flights up to 6 km amsl including into supercooled clouds. Profiling the atmosphere with in situ measurements is important for understanding and predicting local air quality and health effects, at-

360 mospheric transport, and boundary layer meteorology, and can serve as a benchmark against which to validate (ground-based) remote sensing retrievals.

The second application is the characterization of an aerosol plume. Our measurement UAV can fly autonomous measurement missions (Section 5), where it can fly horizontal or vertical transects through a stationary plume, or hover stationary while a plume is passing. In the CLOUDLAB project, we use this approach to characterize the cloud seeding plume, though the UAV

365 can easily be used for characterizing any other type of plume, such as from a factory chimney. The data obtained from such

plume dispersion measurements could help to better map, model, and predict the dispersion and transport of pollution in our atmosphere.

Finally, the third, and most novel, application is glaciogenic cloud seeding with our new seeding UAV. We showed that the seeding UAV can burn a flare containing around 20 g of ice-active seeding material, directly in stratus clouds of below −5 °C.

370 Because our UAVs have a propeller heating system to prevent ice buildup, they are capable of flying in supercooled clouds, which has so far been a major challenge for the use of UAVs in cloud research. CLOUDLAB's cloud seeding experiments were primarily designed for the purpose of investigating ice crystal formation and growth (Henneberger et al., 2023), so it is essential for us to have the ability to seed directly within supercooled clouds, where ice nucleation initiates almost immediately. Its feasibility for operational seeding has not been investigated here and is not a goal of CLOUDLAB. Rather, our seeding method

375 is ideal for researching the microphysical processes of aerosol-cloud interactions and ice crystal growth within persistent stratus clouds. We have shown that not only can we produce a cloud seeding plume from a multirotor UAV, but we can also detect it, and therefore assess the microphysical changes within it (Sect. 5). We also explained our control over parameters like seeding distance, height, and pattern extent. Future work will include using these methods to quantify ice crystal formation and growth in real cloud conditions, as well as to investigate the aerosol-cloud interactions by these seeding particles, namely their

380 hygroscopic growth, cloud droplet activation, and ice nucleating abilities.

Appendix A: POPS size measurement validations

Two POPS validation experiments are presented here: a size validation with monodispersed submicron particles (Fig. A1) and a size and concentration comparison to reference instruments in ambient air (Fig. A2).

Figure A1 shows size distributions from POPS$_{TBS}$ and POPS$_{UAV}$ measuring submicron aerosolized polystyrene latex (PSL)

385 spheres of different sizes, 522 nm and 246 nm, for 60 seconds each. The size distributions illustrate that POPS$_{TBS}$ and POPS$_{UAV}$ both correctly size the PSL particles. Particles measured in other size bins are due to other contaminate substances in the PSL solution and make-up airflow, and both POPS also agree well here, across all size bins. Differences in concentrations in each bin between the POPS$_{TBS}$ and POPS$_{UAV}$ are on average 32% during the 246 nm PSL measurements, and on average 27% during the 522 nm PSL measurements, with a range of 0-110% and 2-88%, respectively. Therefore, we estimate that the instru-

390 ment variability of POPS concentration is 30%, which also indicates at least a 30% uncertainty with all POPS concentration measurements. This is a larger uncertainty than the 20% uncertainty calculated by Mynard et al. (2023) based on flow rate, scattering amplitude, and laser temperature uncertainties, or the 15% uncertainty estimated by Gao et al. (2016) based on Mie resonance uncertainty. Our instrument variability of up to 110% does agree with the comparison in Pilz et al. (2022) with two POPS also having up to 109% variability.

395 Figure A2 shows size distributions from the POPS$_{TBS}$, an Aerodynamic Particle Sizer (APS 3321, TSI), and a Scanning Mobility Particle Sizer (SMPS: electrostatic classifier 3082 with CPC 3787, TSI) while measuring ambient air in the laboratory. SMPS and APS sizes were converted to volume-equivalent diameters, using a shape factor of 1.2 and particle density of $2 \, \text{g cm}^{-3}$, consistent with ambient air estimates (Thomas and Charvet, 2017). Similar to previous studies (Gao et al., 2016;
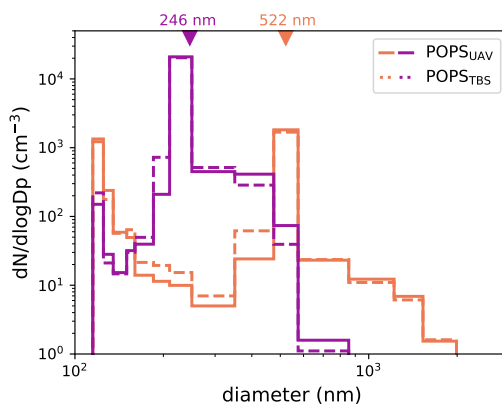
Figure A1. Size distributions from laboratory measurements of aerosolized polystyrene latex (PSL) spheres of size 522 nm (orange) and 246 nm (purple), measured by both the POPS$_{UAV}$ (solid lines) and the POPS$_{TBS}$ (dashed lines). Each size distribution represents 60 seconds of measurement.

Liu et al., 2021; Kasparoglu et al., 2022), POPS$_{TBS}$ ambient air size distributions agree very well with the APS and SMPS in the range where they overlap. Percent differences were calculated for concentrations in each POPS$_{TBS}$ size bin relative to their corresponding reference concentration from the SMPS or APS. The mean percent difference across bins was 50% (range 2 - 103%, no trend with size) which we take as the estimate for the uncertainty in POPS concentrations across the size distribution.
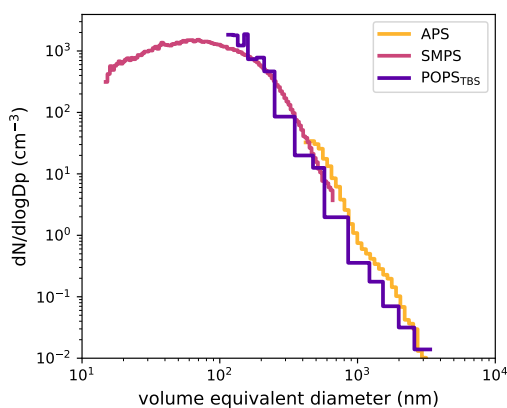
Figure A2. Size distribution with volume equivalent diameter (nm) comparing the POPS$_{TBS}$ (dark purple) to an Aerodynamic Particle Sizer (APS, yellow) and a Scanning Mobility Particle Sizer (SMPS, pink) in ambient lab air over 2.5 hours.

Appendix B: Vertical profiles of boundary layer

Figure B1 shows particle concentration (125 - 3370 nm size range) up to 1950 m amsl (1030 m agl) for the ascent and descent of 34 vertical profile flights of the measurement UAV (flight speed of $10\,\mathrm{m\,s^{-1}}$), conducted on 14 different days, at varying times, in February, March, and December 2022 and January and February 2023 at the main measurement site of the CLOUDLAB project. The boundary layer height can be recognized in many of the profiles where there is a strong negative gradient in particle concentration, e.g., in the profiles of 2022-02-24, 2022-03-04, 2022-03-08, 2023-02-03, and 2023-02-24. In nearly all of the profiles, the ascent and descent measurements are in very good agreement and closely overlap. In the two profiles on 28 January 2022, the descent measurements strongly deviated from the ascent measurements, including several extreme outliers (concentration $> 5000\,\mathrm{cm^{-3}}$); we have no explanation for this, though it was likely caused by an error in the instrument and was not reflective of the true character of the atmosphere. There are similarly few other data points with unusually high concentration, e.g., in 2023-02-03 15:29, and these data can be excluded as outliers. A quantitative comparison of the vertical ascent and descent is discussed in Section 3.2.

Appendix C: Data filter for high concentration POPS data

POPS, like all particle counters, has a concentration threshold above which it does not count and/or size particles accurately (Gao et al., 2016). The main source of uncertainty arises from coincidence errors in particle counting, whereby the scattering signal from one particle overlaps with the scattering signal from the next particle, making it difficult to separate peaks and count two discrete particles. The upper counting limit (software speed limit) of POPS to count every single particle arriving is 10,000 particles $\mathrm{s^{-1}}$, but the counting error is still under 10% up to 20,000 particles $\mathrm{s^{-1}}$ (Gao et al., 2016). When using the recommended flow rate of $3\,\mathrm{cm^3\,s^{-1}}$, this counting limit corresponds to 3,333 particles $\mathrm{cm^{-3}}$, or 6,666 particles $\mathrm{cm^{-3}}$ for up to 90% accuracy. Using a lower flow rate of $0.9\,\mathrm{cm^3\,s^{-1}}$ (the lower end of the possible flow range) results in a counting limit of up to 22,222 particles $\mathrm{cm^{-3}}$, although inaccuracies in counting have not been quantified for flow rates other than the nominal recommended flow rate of $3\,\mathrm{cm^3\,s^{-1}}$.

In our seeding experiments (described in Section 5), we utilize POPS for measuring the seeding plume. However, the seeding plume is emitted at such high concentrations, that it is difficult for us to measure it accurately using POPS. In our later experiments, we measured further downwind in order to sample the plume when its dispersion was larger and concentrations were therefore lower, but in our first set of experiments in 2022, we flew POPS in the very highly concentrated part of the plume (more than $15000\,\mathrm{cm^{-3}}$), highlighting the need for robust filtering to ensure good data quality. One example timeseries of particle concentration from an out-of-cloud seeding mission on 9 March 2023 is shown in Fig. C1c. The concentration peaks occur when the measurement UAV was flown through the seeding plume. Because the flow rate used here was $0.9\,\mathrm{cm^3\,s^{-1}}$, concentration exceeds 14,000 particles $\mathrm{cm^{-3}}$ while counts were exceeding 12,000 $\mathrm{s^{-1}}$. Size distributions for each measurement are shown in Fig. C1a, where each timestep and bin are colored by the bin counts. At many of the high concentration measurements, size distributions showed that particles were not being counted in the smallest size bins, contrary to the expectation that a higher concentration of seeding particles would lead to higher counts in all relevant size bins. These "holes" in the size
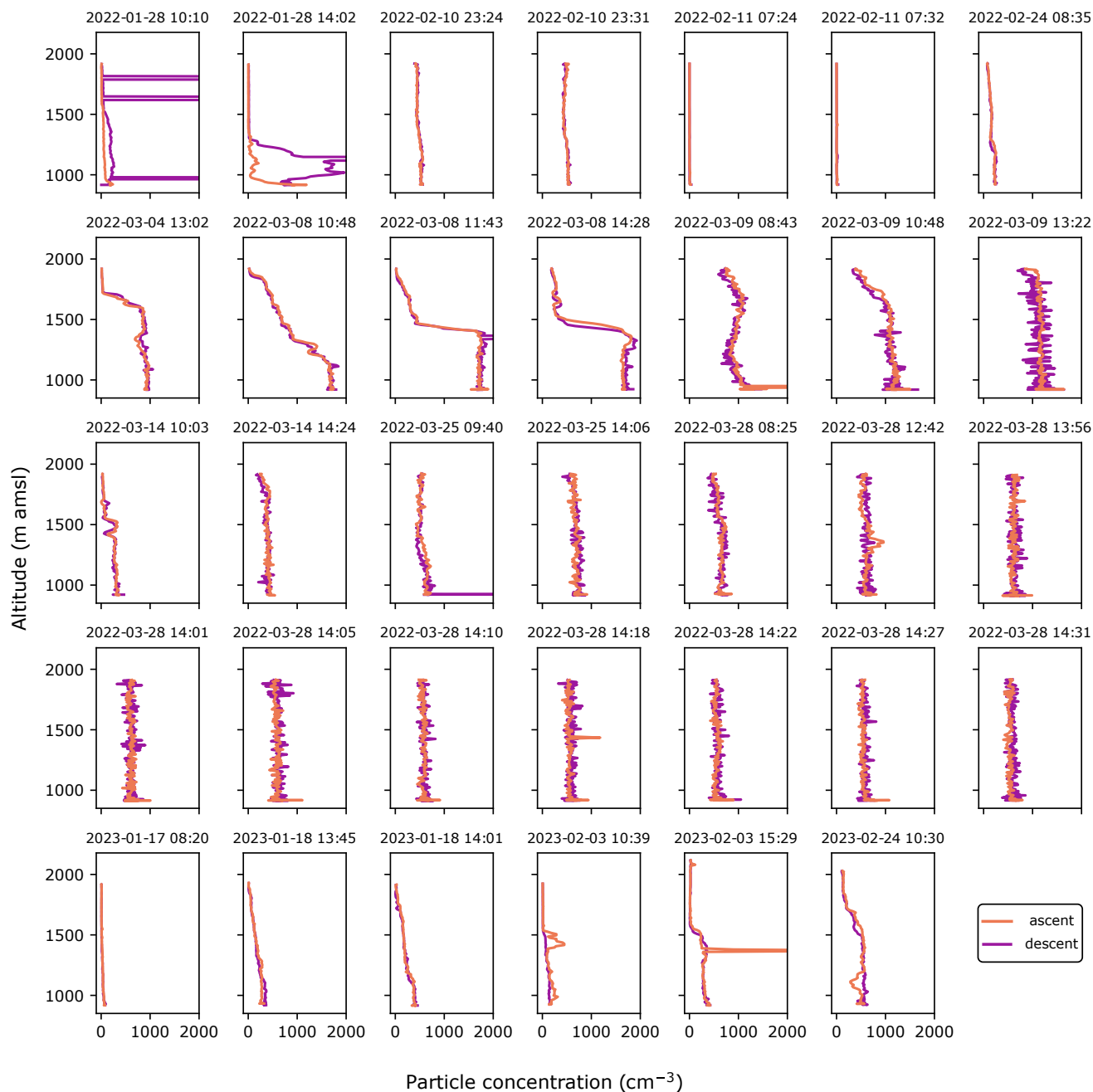
Figure B1. All 34 profiles to 1950 m above sea level (1030 m above ground) performed by the measurement UAV, with ascent (orange) and descent (purple) measurements of particle concentration are shown (125 - 3370 nm size range). The start time of each profile is written above each panel.

https://doi.org/10.5194/amt-2023-157
distribution heatmap (Fig. C1a) indicate that particles were not being sized and counted correctly at very high concentrations within the seeding plume. The likely explanation is that at very high concentrations, there are a high number of large and small particles, and because the large particles have a significantly larger scattering amplitude (scattering amplitude scales with the square of the radius), they block the scattering signals from the smaller particles - essentially, a huge amount of coincidence errors happens at these extremely high concentrations and mainly affect how the smallest particles are sized and counted. It is also possible that many small particles could be miscounted as one larger particle, further affecting the small size bins. The missing counts in the small size bins also indicate that the true total concentration is much higher than the 14,000 particles cm^{-3} recorded. At some measurements of high total concentration, however, there are no "holes" in the size distribution (e.g., at 11:17 - 11:18), suggesting that at these times, the true concentration was lower and particles may have been more accurately counted and sized. The task is then to find which measurements are accurate and which are not.

A parameter that we found useful for assessing the quality of the data is the POPS "baseline" (included in the usual POPS data files) shown in Fig. C1b. The baseline, in units of raw analog-to-digital (A/D) counts, is the background scattering signal received by the detector (i.e., a measure of noise in the data). A particle is counted as a particle only if its scattering signal height is a certain set amount larger than the baseline (default threshold is set to 3 times the baseline standard deviation plus the baseline, e.g., if baseline is 2000 ± 5, then a particle must have a signal of at least 2015 to be counted). When measuring ambient air, the baseline may fluctuate up to $\pm$ 10 from the average. While measuring the seeding plume, however, the baseline can increase up to 800 raw A/D counts higher than the background (Fig. C1b). These increases in baseline correlated with the times when there were "holes" in the size distributions (Fig. C1a): if total (true) concentration increases, then the background scattering signal will also increase, and at some point the background scattering signal will be higher than a small particle scattering signal, such that the small particle will be missed by the counting even if the particle is in the normal size range of what POPS can measure. Therefore, we developed a quality-control method using the baseline values. For each seeding experiment, the median of the baseline for the background (not in the seeding plume) measurements was calculated. The limit for "good data" is taken as the background median baseline + 15, such that any measurements with a baseline higher than this are flagged for exclusion from further analysis. In Figure C1b and c, the raw data and the quality-controlled data are both plotted to show what data is included after filtering. In Figure C1d, an analagous heatmap as in Figure C1a is shown but with only the quality-controlled data (after the filter). Much of the high-concentration measurements from within the plume are removed with this approach. We deem the remaining data with high concentration to be trustworthy because the baseline value is within the appropriate range and the size distribution looks reasonable. The case presented here is one of the more extreme cases we sampled, and many of our seeding experiments do not need so much data removed.

Other studies have suggested setting limits of total concentration to filter out bad data. Mei et al. (2022) flagged data with concentrations above 4000 particles cm^{-3}, while Mynard et al. (2023) flagged data with concentrations above 7000 particles cm^{-3}. However, the concentration measurement itself is biased. The total concentration depends on the counts in each size bin, and if some sizes are categorically not counted, then the concentration will not be reflective of the true concentration. We propose that the baseline be used for quality control because it gives a direct indication of whether the background is too high
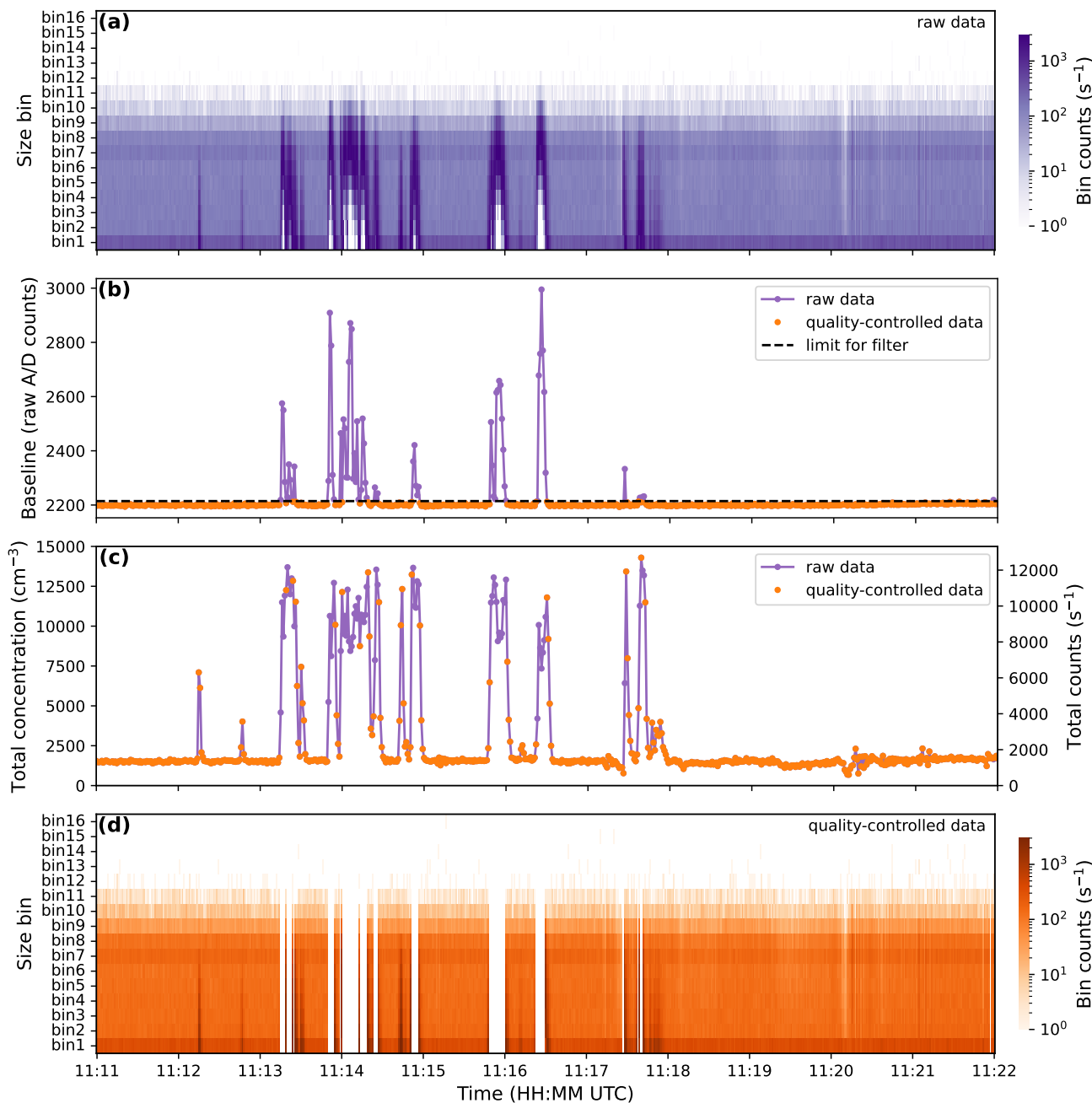
Figure C1. Data filtering for an out-of-cloud seeding mission on 9 March 2022. a) Heatmap timeseries of particle size distributions, with raw data of bin counts per second (color) in each particle size bin (y-axis) at each 1-second timestep (x-axis). b) Timeseries of the POPS baseline, with raw data (blue) and data kept after filtering (quality-controlled data, orange). Black dashed line indicates the baseline value which is taken as the limit for filtering the data, i.e., data is excluded for any time where the baseline is higher than the baseline limit. c) Timeseries of total particle concentration of raw data (blue) and data kept after filtering (orange). d) Heatmap timeseries of particle size distributions (like in a), for only the data kept after filtering.

to count all sizes of particles. With this analysis, we also stress the importance of looking into the size distributions for all measurements, and not only total particle concentration.

Code and data availability. Data and scripts available at XX. Note from authors: Data and scripts will be uploaded into a repository upon acceptance, and are available upon request until then.

475 *Author contributions.* UL, ZAK, JH, FR conceived of the idea of CLOUDLAB and obtained funding. AJM, FR, ZAK, JH contributed in designing the modifications to the UAVs. AJM conducted laboratory validations of POPS. AJM and NO conducted the rotor comparison experiments. AJM, FR, JH designed and conducted the out-of-cloud seeding experiment presented here. AJM, FR, NO, CF, RS, HZ, JH designed and conducted the in-cloud seeding experiment presented here, with conceptual input from UL and ZAK. AJM performed the data analysis of POPS data and created all figures presented here, except for Figure 3 created by FR. AJM wrote the manuscript. All authors
480 contributed to the editing and review of the manuscript.

Competing interests. Zamin A. Kanji is a member of the editorial board of Atmospheric Measurement Techniques. The peer-review process was guided by an independent editor and the authors have no other competing interests.

Acknowledgements. The CLOUDLAB project has received funding from the European Research Council (ERC) 411 under the European Union's Horizon 2020 research and innovation program (grant agreement 412 No. 101021272 CLOUDLAB).
485 The authors would like to sincerely thank and acknowledge: Lukas Hammerschmidt, Daniel Schmitz, Philipp Kryenbühl, Remo Steiner, Dominik Brändle and the other Meteomatics employees for the interactive development of our UAVs including the flight pattern, POPS integration, and flare attachment and ignition, as well as for the valuable expertise, discussions, and prompt assistance with all things related to our Meteodrones; Patric Seifert, Johannes Bühl, Tom Gaudek, Kevin Ohneiser, and Martin Radenz from TROPOS for the remote sensing instrumentation and expertise which helped support the in-cloud seeding experiments; Maxime Hervo and Philipp Baettig from MeteoSwiss
490 for the wind profiler integral to planning experiments; Jürg Wildi and Philip Bärtschi from v2sky for handling the applications for flight permits and Jeroen Kroese, Judith Baumann, and Santiago Llucia from the Federal Office of Civial Aviation (FOCA) for communication and support during the approval process; Michael Rösch for helping design and print the POPS inlets and for making the POPSBox for the TBS platform; Jannis Portmann for assistance in the field with drone flights; Robert David and Toni Klausen for helping with the size validation experiments; Brian Rainwater from Handix Scientific for help and expertise with the POPS technical details; Frank Kasparek and Aleksei
495 Shilin from Cloud seeding Technologies for discussions about the seeding flares; the Swiss army and the Gütergemeinde Hinterdorf Eriswil for allowing us to use their property and giving us a base; Stefan Minder for the maintenance of our base; and finally, all the farmers around Eriswil who graciously let us use their land as drone launching locations at all hours of the night and day.

References

Al Hosari, T., Al Mandous, A., Wehbe, Y., Shalaby, A., Al Shamsi, N., Al Naqbi, H., Al Yazeedi, O., Al Mazroui, A., and Farrah, S.: The UAE
Cloud Seeding Program: A Statistical and Physical Evaluation, Atmosphere, 12, 1013–1030, https://doi.org/10.3390/atmos12081013,
2021.

Alaoui-Sosse, S., Durand, P., Medina, P., Pastor, P., Lothon, M., and Cernov, I.: OVLI-TA: An Unmanned Aerial System for Measuring
Profiles and Turbulence in the Atmospheric Boundary Layer, Sensors, 19, 581–602, https://doi.org/10.3390/s19030581, 2019.

Albadra, A., Wood, K., Berthoud, L., Calway, A., Watson, M., Thomas, H., Richardson, T., Liu, E., and Chigna, G.: Determining the Three-
Dimensional Structure of a Volcanic Plume Using Unoccupied Aerial System (UAS) Imagery, Journal of Volcanology and Geothermal
Research, 407, 106 731–106 741, https://doi.org/10.1016/j.jvolgeores.2019.106731, 2020.

Alvarado, M., Gonzalez, F., Erskine, P., Cliff, D., and Heuff, D.: A Methodology to Monitor Airborne PM10 Dust Particles Using a Small
Unmanned Aerial Vehicle, Sensors, 17, 343–368, https://doi.org/10.3390/s17020343, 2017.

Bärfuss, K. B., Schmithüsen, H., and Lampert, A.: Drone-Based Meteorological Observations up to the Tropopause, Atmospheric Measure-
ment Techniques Discussions, pp. 1–26, https://doi.org/10.5194/amt-2022-236, 2022.

Benjamini, Y., Givati, A., Khain, P., Levi, Y., Rosenfeld, D., Shamir, U., Siegel, A., Zipori, A., Ziv, B., and Steinberg, D. M.:
The Israel 4 Cloud Seeding Experiment: Primary Results, Journal of Applied Meteorology and Climatology, 62, 317–327,
https://doi.org/10.1175/JAMC-D-22-0077.1, 2023.

Bernstein, B. C., McDonough, F., Politovich, M. K., Brown, B. G., Ratvasky, T. P., Miller, D. R., Wolff, C. A., and Cunning, G.: Current
Icing Potential: Algorithm Description and Comparison with Aircraft Observations, Journal of Applied Meteorology (1988-2005), 44,
969–986, https://doi.org/10.1175/JAM2246.1, 2005.

Brockmann, J. E.: Aerosol Transport in Sampling Lines and Inlets, in: Aerosol Measurement: Principles, Techniques, and Appli-
cations, edited by Kulkarni, P., Baron, P. A., and Willeke, K., pp. 69–106, John Wiley & Sons, Ltd, Hoboken, N.J, 3 edn.,
https://doi.org/10.1002/9781118001684, 2011.

Brosy, C., Krampf, K., Zeeman, M., Wolf, B., Junkermann, W., Schäfer, K., Emeis, S., and Kunstmann, H.: Simultaneous
Multicopter-Based Air Sampling and Sensing of Meteorological Variables, Atmospheric Measurement Techniques, 10, 2773–2784,
https://doi.org/10.5194/amt-10-2773-2017, 2017.

Bruintjes, R. T.: A Review of Cloud Seeding Experiments to Enhance Precipitation and Some New Prospects, Bulletin of the American
Meteorological Society, 80, 805–820, https://doi.org/10.1175/1520-0477(1999)080<0805:AROCSE>2.0.CO;2, 1999.

Brus, D., Gustafsson, J., Kemppinen, O., de Boer, G., and Hirsikko, A.: Atmospheric Aerosol, Gases, and Meteorological Parameters Mea-
sured during the LAPSE-RATE Campaign by the Finnish Meteorological Institute and Kansas State University, Earth System Science
Data, 13, 2909–2922, https://doi.org/10.5194/essd-13-2909-2021, 2021.

Catry, G., Ceyhan, O., Noca, F., Bosson, N., Bardazzi, L. J., Marquez, S., Jordaens, P. J., and Brandolisio, D.: Performance Analysis of
Rotorcraft Propulsion Units in a Combination of Wind and Icing Conditions, in: AIAA AVIATION 2021 FORUM, American Institute of
Aeronautics and Astronautics, Virtual Event, https://doi.org/10.2514/6.2021-2677, 2021.

Collaud Coen, M., Praz, C., Haefele, A., Ruffieux, D., Kaufmann, P., and Calpini, B.: Determination and Climatology of the Planetary
Boundary Layer Height above the Swiss Plateau by in Situ and Remote Sensing Measurements as Well as by the COSMO-2 Model,
Atmospheric Chemistry and Physics, 14, 13 205–13 221, https://doi.org/10.5194/acp-14-13205-2014, 2014.

Creamean, J. M., de Boer, G., Telg, H., Mei, F., Dexheimer, D., Shupe, M. D., Solomon, A., and McComiskey, A.: Assessing the
    Vertical Structure of Arctic Aerosols Using Balloon-Borne Measurements, Atmospheric Chemistry and Physics, 21, 1737–1757,
    https://doi.org/10.5194/acp-21-1737-2021, 2021.

de Boer, G., Ivey, M., Schmid, B., Lawrence, D., Dexheimer, D., Mei, F., Hubbe, J., Bendure, A., Hardesty, J., Shupe, M. D., McComiskey,
    A., Telg, H., Schmitt, C., Matrosov, S. Y., Brooks, I., Creamean, J., Solomon, A., Turner, D. D., Williams, C., Maahn, M., Argrow, B., Palo,
    S., Long, C. N., Gao, R.-S., and Mather, J.: A Bird's-Eye View: Development of an Operational ARM Unmanned Aerial Capability for
    Atmospheric Research in Arctic Alaska, Bulletin of the American Meteorological Society, 99, 1197–1212, https://doi.org/10.1175/BAMS-
    D-17-0156.1, 2018.

DeFelice, T. P., Axisa, D., Bird, J. J., Hirst, C. A., Frew, E. W., Burger, R. P., Baumgardner, D., Botha, G., Havenga, H., Breed, D.,
    Bornstein, S., Choate, C., Gomez-Faulk, C., and Rhodes, M.: Modern and Prospective Technologies for Weather Modification Ac-
    tivities: A First Demonstration of Integrating Autonomous Uncrewed Aircraft Systems, Atmospheric Research, 290, 106 788–106 800,
    https://doi.org/10.1016/j.atmosres.2023.106788, 2023.

Dennis, A. S.: Weather Modification by Cloud Seeding, vol. 24 of *International Geophysics Series*, Academic Press, Inc., New York, https:
    //digitalcommons.usu.edu/water_rep/670, 1980.

Egerer, U., Cassano, J. J., Shupe, M. D., de Boer, G., Lawrence, D., Doddi, A., Siebert, H., Jozef, G., Calmer, R., Hamilton, J., Pilz, C., and
    Lonardi, M.: Estimating Turbulent Energy Flux Vertical Profiles from Uncrewed Aircraft System Measurements: Exemplary Results for
    the MOSAiC Campaign, Atmospheric Measurement Techniques, 16, 2297–2317, https://doi.org/10.5194/amt-16-2297-2023, 2023.

French, J. R., Friedrich, K., Tessendorf, S. A., Rauber, R. M., Geerts, B., Rasmussen, R. M., Xue, L., Kunkel, M. L., and Blestrud,
    D. R.: Precipitation Formation from Orographic Cloud Seeding, Proceedings of the National Academy of Sciences, 115, 1168–1173,
    https://doi.org/10.1073/pnas.1716995115, 2018.

Friedrich, K., French, J. R., Tessendorf, S. A., Hatt, M., Weeks, C., Rauber, R. M., Geerts, B., Xue, L., Rasmussen, R. M., Blestrud, D. R.,
    Kunkel, M. L., Dawson, N., and Parkinson, S.: Microphysical Characteristics and Evolution of Seeded Orographic Clouds, Journal of
    Applied Meteorology and Climatology, 60, 909–934, https://doi.org/10.1175/JAMC-D-20-0206.1, 2021.

Fuertes, F. C., Wilhelm, L., and Porté-Agel, F.: Multirotor UAV-Based Platform for the Measurement of Atmospheric Turbulence: Valida-
    tion and Signature Detection of Tip Vortices of Wind Turbine Blades, Journal of Atmospheric and Oceanic Technology, 36, 941–955,
    https://doi.org/10.1175/JTECH-D-17-0220.1, 2019.

Gao, R. S., Telg, H., McLaughlin, R. J., Ciciora, S. J., Watts, L. A., Richardson, M. S., Schwarz, J. P., Perring, A. E., Thornberry, T. D.,
    Rollins, A. W., Markovic, M. Z., Bates, T. S., Johnson, J. E., and Fahey, D. W.: A Light-Weight, High-Sensitivity Particle Spectrometer
    for PM2.5 Aerosol Measurements, Aerosol Science and Technology, 50, 88–99, https://doi.org/10.1080/02786826.2015.1131809, 2016.

Griffith, D. A., Solak, M. E., and Yorty, D. P.: 30+ Winter Seasons Of Operational Cloud Seeding In Utah, The Journal of Weather Modifi-
    cation, 41, 23–37, https://doi.org/10.54782/jwm.v41i1.175, 2009.

Henneberger, J., Ramelli, F., Spirig, R., Omanovic, N., Miller, A. J., Fuchs, C., Zhang, H., Bühl, J., Hervo, M., Kanji, Z. A., Ohneiser, K.,
    Radenz, M., Rösch, M., Seifert, P., and Lohmann, U.: Seeding of Supercooled Low Stratus Clouds with a UAV to Study Microphysical
    Ice Processes - An Introduction to the CLOUDLAB Project, Bulletin of the American Meteorological Society, in review, 2023.

Heymsfield, A. J., Schmitt, C., Chen, C.-C.-J., Bansemer, A., Gettelman, A., Field, P. R., and Liu, C.: Contributions of the Liquid and Ice
    Phases to Global Surface Precipitation: Observations and Global Climate Modeling, Journal of the Atmospheric Sciences, 77, 2629–2648,
    https://doi.org/10.1175/JAS-D-19-0352.1, 2020.

Holland, G. J., Webster, P. J., Curry, J. A., Tyrell, G., Gauntlett, D., Brett, G., Becker, J., Hoag, R., and Vaglienti, W.: The Aerosonde Robotic Aircraft: A New Paradigm for Environmental Observations, Bulletin of the American Meteorological Society, 82, 889–902, https://doi.org/10.1175/1520-0477(2001)082<0889:TARAAN>2.3.CO;2, 2001.

Holmes, N. and Morawska, L.: A Review of Dispersion Modelling and Its Application to the Dispersion of Particles: An Overview of
575   Different Dispersion Models Available, Atmospheric Environment, 40, 5902–5928, https://doi.org/10.1016/j.atmosenv.2006.06.003, 2006.

Järvi, L., Kurppa, M., Kuuluvainen, H., Rönkkö, T., Karttunen, S., Balling, A., Timonen, H., Niemi, J. V., and Pirjola, L.: Determinants of Spatial Variability of Air Pollutant Concentrations in a Street Canyon Network Measured Using a Mobile Laboratory and a Drone, Science of The Total Environment, 856, 158 974–158 988, https://doi.org/10.1016/j.scitotenv.2022.158974, 2023.

Jozef, G., Cassano, J., Dahlke, S., and de Boer, G.: Testing the Efficacy of Atmospheric Boundary Layer Height Detection Algorithms Using
580   Uncrewed Aircraft System Data from MOSAiC, Atmospheric Measurement Techniques, 15, 4001–4022, https://doi.org/10.5194/amt-15-4001-2022, 2022.

Jung, W., Cha, J. W., Ko, A.-R., Chae, S., Ro, Y., Hwang, H. J., Kim, B.-Y., Ku, J. M., Chang, K.-H., and Lee, C.: Progressive and Prospective Technology for Cloud Seeding Experiment by Unmanned Aerial Vehicle and Atmospheric Research Aircraft in Korea, Advances in Meteorology, 2022, 1–14, https://doi.org/10.1155/2022/3128657, 2022.

585   Kanji, Z. A., Ladino, L. A., Wex, H., Boose, Y., Burkert-Kohn, M., Cziczo, D. J., and Krämer, M.: Overview of Ice Nucleating Particles, Meteorological Monographs, 58, 1.1–1.33, https://doi.org/10.1175/AMSMONOGRAPHS-D-16-0006.1, 2017.

Kasparoglu, S., Islam, M. M., Meskhidze, N., and Petters, M. D.: Characterization of a Modified Printed Optical Particle Spectrometer for High-Frequency and High-Precision Laboratory and Field Measurements, Atmospheric Measurement Techniques, 15, 5007–5018, https://doi.org/10.5194/amt-15-5007-2022, 2022.

590   Kezoudi, M., Keleshis, C., Antoniou, P., Biskos, G., Bronz, M., Constantinides, C., Desservettaz, M., Gao, R.-S., Girdwood, J., Harnetiaux, J., Kandler, K., Leonidou, A., Liu, Y., Lelieveld, J., Marenco, F., Mihalopoulos, N., Močnik, G., Neitola, K., Paris, J.-D., Pikridas, M., Sarda-Esteve, R., Stopford, C., Unga, F., Vrekoussis, M., and Sciare, J.: The Unmanned Systems Research Laboratory (USRL): A New Facility for UAV-Based Atmospheric Observations, Atmosphere, 12, 1042–1077, https://doi.org/10.3390/atmos12081042, 2021.

Kloss, C., Sellitto, P., Legras, B., Vernier, J.-P., Jégou, F., Venkat Ratnam, M., Suneel Kumar, B., Lakshmi Madhavan, B., and Berthet,
595   G.: Impact of the 2018 Ambae Eruption on the Global Stratospheric Aerosol Layer and Climate, Journal of Geophysical Research: Atmospheres, 125, e2020JD032 410, https://doi.org/10.1029/2020JD032410, 2020.

Knopf, D. A. and Alpert, P. A.: Atmospheric Ice Nucleation, Nature Reviews Physics, pp. 1–15, https://doi.org/10.1038/s42254-023-00570-7, 2023.

Koch, S. E., Fengler, M., Chilson, P. B., Elmore, K. L., Argrow, B., Andra, D. L., and Lindley, T.: On the Use of Unmanned Aircraft for
600   Sampling Mesoscale Phenomena in the Preconvective Boundary Layer, Journal of Atmospheric and Oceanic Technology, 35, 2265–2288, https://doi.org/10.1175/JTECH-D-18-0101.1, 2018.

Kulkarni, J., Morwal, S., and Deshpande, N.: Rainfall Enhancement in Karnataka State Cloud Seeding Program "Varshadhare" 2017, Atmospheric Research, 219, 65–76, https://doi.org/10.1016/j.atmosres.2018.12.020, 2019.

Lata, N. N., Cheng, Z., Dexheimer, D., Zhang, D., Mei, F., and China, S.: Vertical Gradient of Size-Resolved Aerosol Compositions
605   over the Arctic Reveals Cloud Processed Aerosol in-Cloud and above Cloud, Environmental Science & Technology, 57, 5821–5830, https://doi.org/10.1021/acs.est.2c09498, 2023.

Leuenberger, D., Haefele, A., Omanovic, N., Fengler, M., Martucci, G., Calpini, B., Fuhrer, O., and Rossa, A.: Improving High-Impact Numerical Weather Prediction with Lidar and Drone Observations, Bulletin of the American Meteorological Society, 101, E1036–E1051, https://doi.org/10.1175/BAMS-D-19-0119.1, 2020.

610 Li, S., Xing, M., Jiang, L., Chen, P., Ding, F., and Yang, W.: Vertical Variation of Atmospheric Particulate Matter under Different Pollution Levels in the Suburbs of Tianjin Based on Unmanned Aerial Vehicle, Journal of the Air & Waste Management Association, 72, 1463–1476, https://doi.org/10.1080/10962247.2022.2134231, 2022.

Liu, Z., Osborne, M., Anderson, K., Shutler, J. D., Wilson, A., Langridge, J., Yim, S. H. L., Coe, H., Babu, S., Satheesh, S. K., Zuidema, P., Huang, T., Cheng, J. C. H., and Haywood, J.: Characterizing the Performance of a POPS Miniaturized Optical Particle Counter When

615 Operated on a Quadcopter Drone, Atmospheric Measurement Techniques, 14, 6101–6118, https://doi.org/10.5194/amt-14-6101-2021, 2021.

Mamali, D., Marinou, E., Sciare, J., Pikridas, M., Kokkalis, P., Kottas, M., Binietoglou, I., Tsekeri, A., Keleshis, C., Engelmann, R., Baars, H., Ansmann, A., Amiridis, V., Russchenberg, H., and Biskos, G.: Vertical Profiles of Aerosol Mass Concentration Derived by Unmanned Airborne in Situ and Remote Sensing Instruments during Dust Events, Atmospheric Measurement Techniques, 11, 2897–2910,

620 https://doi.org/10.5194/amt-11-2897-2018, 2018.

McGonigle, A. J. S., Aiuppa, A., Giudice, G., Tamburello, G., Hodson, A. J., and Gurrieri, S.: Unmanned Aerial Vehicle Measurements of Volcanic Carbon Dioxide Fluxes, Geophysical Research Letters, 35, 1–4, https://doi.org/10.1029/2007GL032508, 2008.

Mei, F., McMeeking, G., Pekour, M., Gao, R.-S., Kulkarni, G., China, S., Telg, H., Dexheimer, D., Tomlinson, J., and Schmid, B.: Performance Assessment of Portable Optical Particle Spectrometer (POPS), Sensors, 20, 6294–6316, https://doi.org/10.3390/s20216294, 2020.

625 Mei, F., Pekour, M. S., Dexheimer, D., de Boer, G., Cook, R., Tomlinson, J., Schmid, B., Goldberger, L. A., Newsom, R., and Fast, J. D.: Observational Data from Uncrewed Systems over Southern Great Plains, Earth System Science Data, 14, 3423–3438, https://doi.org/10.5194/essd-14-3423-2022, 2022.

Mori, T., Hashimoto, T., Terada, A., Yoshimoto, M., Kazahaya, R., Shinohara, H., and Tanaka, R.: Volcanic Plume Measurements Using a UAV for the 2014 Mt. Ontake Eruption, Earth, Planets and Space, 68, 1–18, https://doi.org/10.1186/s40623-016-0418-0, 2016.

630 Müller, N. C., Løw-Hansen, B., Borup, K. T., and Hann, R.: UAV Icing: Development of an Ice Protection System for the Propeller of a Small UAV, Cold Regions Science and Technology, 213, 103 938–103 953, https://doi.org/10.1016/j.coldregions.2023.103938, 2023.

Mülmenstädt, J., Sourdeval, O., Delanoë, J., and Quaas, J.: Frequency of Occurrence of Rain from Liquid-, Mixed-, and Ice-Phase Clouds Derived from A-Train Satellite Retrievals, Geophysical Research Letters, 42, 6502–6509, https://doi.org/10.1002/2015GL064604, 2015.

Mynard, A., Kent, J., Smith, E. R., Wilson, A., Wivell, K., Nelson, N., Hort, M., Bowles, J., Tiddeman, D., Langridge, J. M., Drummond, B.,

635 and Abel, S. J.: Long-Term Airborne Measurements of Pollutants over the UK, Including during the COVID-19 Pandemic, to Support Air Quality Model Development and Evaluation, Atmospheric Measurement Techniques Discussions, pp. 1–52, https://doi.org/10.5194/amt-2023-15, 2023.

Pilz, C., Düsing, S., Wehner, B., Müller, T., Siebert, H., Voigtländer, J., and Lonardi, M.: CAMP: An Instrumented Platform for Balloon-Borne Aerosol Particle Studies in the Lower Atmosphere, Atmospheric Measurement Techniques, 15, 6889–6905, https://doi.org/10.5194/amt-

640 15-6889-2022, 2022.

Pusfitasari, E. D., Ruiz-Jimenez, J., Tiusanen, A., Suuronen, M., Haataja, J., Wu, Y., Kangasluoma, J., Luoma, K., Petäjä, T., Jussila, M., Hartonen, K., and Riekkola, M.-L.: Vertical Profiles of Volatile Organic Compounds and Fine Particles in Atmospheric Air by Using an Aerial Drone with Miniaturized Samplers and Portable Devices, Atmospheric Chemistry and Physics, 23, 5885–5904, https://doi.org/10.5194/acp-23-5885-2023, 2023.

645 Ramelli, F., Beck, A., Henneberger, J., and Lohmann, U.: Using a Holographic Imager on a Tethered Balloon System for Microphysical Observations of Boundary Layer Clouds, Atmospheric Measurement Techniques, 13, 925–939, https://doi.org/10.5194/amt-13-925-2020, 2020.

Rauber, R. M., Geerts, B., Xue, L., French, J., Friedrich, K., Rasmussen, R. M., Tessendorf, S. A., Blestrud, D. R., Kunkel, M. L., and Parkinson, S.: Wintertime Orographic Cloud Seeding—A Review, Journal of Applied Meteorology and Climatology, 58, 2117–2140,

650 https://doi.org/10.1175/JAMC-D-18-0341.1, 2019.

Reuder, J., Brisset, P., Jonassen, M. M., and Mayer, S.: The Small Unmanned Meteorological Observer SUMO: A New Tool for Atmospheric Boundary Layer Research, Meteorologische Zeitschrift, 18, 141–147, https://doi.org/10.1127/0941-2948/2009/0363, 2009.

Samad, A., Alvarez Florez, D., Chourdakis, I., and Vogt, U.: Concept of Using an Unmanned Aerial Vehicle (UAV) for 3D Investigation of Air Quality in the Atmosphere—Example of Measurements Near a Roadside, Atmosphere, 13, 663–685,

655 https://doi.org/10.3390/atmos13050663, 2022.

Schaefer, V. J.: The Production of Ice Crystals in a Cloud of Supercooled Water Droplets, Science, 104, 457–549, https://doi.org/10.1126/science.104.2707.457, 1946.

Shirolkar, J., Coimbra, C., and Queiroz McQuay, M.: Fundamental Aspects of Modeling Turbulent Particle Dispersion in Dilute Flows, Progress in Energy and Combustion Science, 22, 363–399, https://doi.org/10.1016/S0360-1285(96)00006-8, 1996.

660 Suchanek, G., Wołoszyn, J., and Gołaś, A.: Evaluation of Selected Algorithms for Air Pollution Source Localisation Using Drones, Sustainability, 14, 3049–3068, https://doi.org/10.3390/su14053049, 2022.

Summa, D., Madonna, F., Franco, N., De Rosa, B., and Di Girolamo, P.: Inter-Comparison of Atmospheric Boundary Layer (ABL) Height Estimates from Different Profiling Sensors and Models in the Framework of HyMeX-SOP1, Atmospheric Measurement Techniques, 15, 4153–4170, https://doi.org/10.5194/amt-15-4153-2022, 2022.

665 Telg, H., Murphy, D. M., Bates, T. S., Johnson, J. E., Quinn, P. K., Giardi, F., and Gao, R.-S.: A Practical Set of Miniaturized Instruments for Vertical Profiling of Aerosol Physical Properties, Aerosol Science and Technology, 51, 715–723, https://doi.org/10.1080/02786826.2017.1296103, 2017.

Thomas, D. and Charvet, A.: An Introduction to Aerosols, in: Aerosol Filtration, edited by Falk, L., pp. 1–30, ISTE Press, London, https://doi.org/10.1016/B978-1-78548-215-1.50001-9, 2017.

670 Vonnegut, B.: The Nucleation of Ice Formation by Silver Iodide, Journal of Applied Physics, 18, 593–595, https://doi.org/10.1063/1.1697813, 1947.

Walter, P., Flynn, J., Sheesley, R., Usenko, S., and Guagenti, M.: TRACER-Tethersonde Field Campaign Report, Tech. Rep. DOE/SC-ARM-23-007, U.S. Department of Energy, Atmospheric Radiation Measurement user facility, Richland, Washington, 2023.

Wang, W., Yao, Z., Guo, J., Tan, C., Jia, S., Zhao, W., Zhang, P., and Gao, L.: The Extra-Area Effect in 71 Cloud Seeding Operations during

675 Winters of 2008–14 over Jiangxi Province, East China, Journal of Meteorological Research, 33, 528–539, https://doi.org/10.1007/s13351-019-8122-1, 2019.

Weber, K., Heweling, G., Fischer, C., and Lange, M.: The Use of an Octocopter UAV for the Determination of Air Pollutants – a Case Study of the Traffic Induced Pollution Plume around a River Bridge in Duesseldorf, Germany, International Journal of Environmental Sciences, 2, 63–66, 2017.

680 WMO: Peer Review Report on Global Precipitation Enhancement Activities, Tech. Rep. WWRP 2018 - 1, World Meteorological Organization, https://library.wmo.int/index.php?lvl=notice_display&id=21531, 2018.

Woodley, W. and Rosenfeld, D.: The Development and Testing of a New Method to Evaluate the Operational Cloud-Seeding Programs in Texas, Journal of Applied Meteorology and Climatology, 43, 249–263, https://doi.org/10.1175/1520-0450(2004)043<0249:TDATOA>2.0.CO;2, 2004.

685   Yu, P., Rosenlof, K. H., Liu, S., Telg, H., Thornberry, T. D., Rollins, A. W., Portmann, R. W., Bai, Z., Ray, E. A., Duan, Y., Pan, L. L., Toon, O. B., Bian, J., and Gao, R.-S.: Efficient Transport of Tropospheric Aerosol into the Stratosphere via the Asian Summer Monsoon Anticyclone, Proceedings of the National Academy of Sciences, 114, 6972–6977, https://doi.org/10.1073/pnas.1701170114, 2017.

Yu, P., Toon, O. B., Bardeen, C. G., Zhu, Y., Rosenlof, K. H., Portmann, R. W., Thornberry, T. D., Gao, R.-S., Davis, S. M., Wolf, E. T., de Gouw, J., Peterson, D. A., Fromm, M. D., and Robock, A.: Black Carbon Lofts Wildfire Smoke High into the Stratosphere to Form a

690   Persistent Plume, Science, 365, 587–590, https://doi.org/10.1126/science.aax1748, 2019.